Atmospheric
Measurement
Techniques
Discussions

The Surface Longwave Cloud Radiative Effect derived from Space Lidar Observations

Assia Arouf[1], Hélène Chepfer[1], Thibault Vaillant de Guélis[2,3], Marjolaine Chiriaco[4], Matthew D. Shupe[5,6], Rodrigo Guzman[1], Artem Feofilov[1], Patrick Raberanto[7], Tristan S. L'Ecuyer[8], Seiji Kato[3], and Michael R. Gallagher[5,6]

[1]LMD/IPSL, Sorbonne Université, École Polytechnique, Institut Polytechnique de Paris, ENS, PSL Université, CNRS, Palaiseau France
[2]Science Systems and Applications, Inc., Hampton, Virginia, USA
[3]NASA Langley Research Center, Hampton, Virginia, USA
[4]LATMOS/IPSL, UVSQ, Université Paris-Saclay, Sorbonne Université, CNRS, 78280, Guyancourt, France
[5]Cooperative Institute for Research in Environmental Sciences, University of Colorado, Boulder, Colorado, USA
[6]NOAA Physical Sciences Laboratory, Boulder, Colorado, USA
[7]LMD/IPSL, CNRS, Sorbonne Université, École Polytechnique, Institut Polytechnique de Paris, ENS, PSL Université, Palaiseau France
[8]Department of Atmospheric and Oceanic Sciences, University of Wisconsin-Madison, USA

Correspondence to: Assia Arouf (assia.arouf@lmd.ipsl.fr)

Abstract. Clouds warm the surface in the longwave (LW) and this warming effect can be quantified through the surface LW cloud radiative effect (CRE). The global surface LW CRE is estimated using long-term observations from space-based radiometers (2000–2021) but has some bias over continents and icy surfaces. It is also estimated globally using the combination of radar, lidar and space-based radiometer over the 5–year period ending in 2011. To develop a more reliable long time series of surface LW CRE over continental and icy surfaces, we propose new estimates of the global surface LW CRE from space-based lidar observations. We show from 1D atmospheric column radiative transfer calculations, that surface LW CRE linearly decreases with increasing cloud altitude. These computations allow us to establish simple relationships between surface LW CRE, and five cloud properties that are well observed by the CALIPSO space-based lidar: opaque cloud cover and altitude, and thin cloud cover, altitude, and emissivity. We use these relationships to retrieve the surface LW CRE at global scale over the 2008–2020 time period (27 Wm^{-2}). We evaluate this new surface LW CRE product by comparing it to existing satellite-derived products globally on instantaneous collocated data at footprint scale and on global averages, as well as to ground-based observations at specific locations. Our estimate appears to be an improvement over others as it appropriately capture the surface LW CRE annual variability over bright polar surfaces and it provides a dataset of more than 13 years long.

1 Introduction

Small changes in the surface irradiance may lead to large climatological responses (Chylek et al., 2007; Kwok and
35   Untersteiner, 2011). Therefore, quantifying irradiance at the Earth's surface is a useful step to better understand the climate
system. Clouds exert a very important effect on the energy balance at the surface of the Earth through their effects on
shortwave (SW) and longwave (LW) radiation. They radiatively warm the surface in the LW domain because they absorb
upward LW radiation that would otherwise escape the Earth system and reemit it back towards the surface. They cool the
surface in the SW domain because they reflect solar radiation back to space that would otherwise partly be absorbed by the
40   surface. These effects are usually quantified using the surface cloud radiative effect (CRE), defined as the change in the SW
and LW radiation reaching the surface induced by the presence of clouds. Globally, clouds radiatively cool the Earth's
surface by 20 W m^{-2} according to Kato et al. (2018) and by 25 W m^{-2} according to L'Ecuyer et al. (2019), with the (negative)
surface SW CRE cooling being two times larger in magnitude than the (positive) surface LW CRE warming. Nevertheless,
in some specific regions like at high latitudes or over the tropical ocean below persistent stratocumulus clouds, the surface
45   LW CRE warming can be larger than the surface SW CRE cooling, such that the clouds exert a net radiative warming of the
surface.

As an example, SW effects vanish in the winter-hemisphere polar regions, leading to positive net CRE as LW effects
dominate (Henderson et al., 2013). While climate warming in the Arctic is already visible with the sea ice melting (Stroeve
et al., 2011), previous works showed that clouds may exert some control on future Arctic climate trajectories (Kay et al.,
50   2016) because they play a primary role in regulating the surface energy balance (Ramanathan et al., 1989; Curry et al., 1996,
Shupe and Intrieri, 2004) which influences the surface melting (van den Broeke et al., 2009). Over Greenland specifically,
van Tricht et al. (2016) showed that clouds increase the radiative fluxes into the surface and therefore could modulate the
Greenland ice sheet mass balance (van Tricht et al., 2016; Hofer et al., 2017), which is a large contributor to global sea-level
rise (Shepherd et al., 2012; IPCC, 2021). In the Southern high latitudes, clouds likely exert an important role on the surface
55   energy budget of Antarctica (Shepherd et al., 2012; Kopp et al., 2016), but their radiative impact in this region remains
largely unexplored (Scott et al., 2017), in spite of the fact that Antarctica contains the largest reservoir of ice on Earth. King
et al. (2015) showed large errors in Antarctic surface energy budget and surface melting rates in models and underlined the
importance of improving observations of cloud radiative properties in this region.

Acquaotta et al. (2014) underlined the current urgent need to develop long term reliable and high-quality climatic time series,
60   in order to better understand, detect, predict and react to global climate variability and change. Given the importance of the
surface LW CRE and the need of long time series, it is necessary to get reliable estimates of the surface LW CRE over
multiple years, everywhere around the globe including over continents and ice-covered regions. The main motivation for the
current work is to derive a long time series of the global surface LW CRE that can be used to better understand the cloud
property that have driven the evolution of the surface LW CRE during the last decade (Vaillant de Guélis et al., 2017b,
65   Norris et al., 2016). This is a necessary step toward understanding how clouds might interact with the surface in the future as

the climate warms (Lindzen and Choi 2021). The ideal way to observe cloud variability everywhere is to combine space radar and space lidar observations (Henderson et al., 2013) because passive sensors often struggle to distinguish clouds from the surface over continents and ice-covered regions. The launch of Cloud-Aerosol Lidar and Infrared Pathfinder Satellite Observations (CALIPSO; Winker et al., 2010) and CloudSat Profiling Radar (CPR; Stephens et al., 2008) in 2006 provided

70   the first opportunity to incorporate information about the global vertical cloud distribution (Henderson et al., 2013) over all surface types and that is an important parameter for surface LW CRE estimates from space. As CloudSat experienced a battery anomaly that limited future observations to daytime scenes only in 2011, CALIPSO's global observations collected since 2006 are the main tool to provide information on the cloud vertical distribution over more than a decade. Therefore, we retrieve the surface LW CRE from space lidar alone over 13 years.

75   Section 2 presents the satellite and ground-based data used in this study. In section 3, we present the method followed to retrieve the surface LW CRE from radiative transfer computations. In section 4, we present the radiative-transfer-based statistical regressions tying the surface LW CRE to cloud altitude and emissivity. In section 5, we present the new surface LW CRE retrieved from the analytical relationships and CALIPSO space-based lidar observations (cloud cover, cloud altitude, and cloud opacity). In section 6, we evaluate this new surface LW CRE product at footprint scale and the gridded

80   product against existing independent surface LW CRE satellite-derived products and against ground-based observations. In section 7, we analyze the variations of the surface LW CRE and we present a long time series of the surface LW CRE retrieved from the radiative transfer computations and space-based lidar observations. Section 8 summarizes the main results and perspectives of this work.

2 Data

This section describes the CALIPSO cloud observations used to retrieve the surface LW CRE and the independent space-based and ground-based datasets used to evaluate it.

2.1 Cloud observations from CALIPSO–GOCCP

We use cloud properties from the GCM Oriented CALIPSO Cloud Product (GOCCP v3.1.2; Chepfer et al., 2010; Cesana et al., 2012; Guzman et al., 2017) over the period 2008–2020. We do not use data collected between 2006 and 2007 because the laser tilted off nadir in November 2007, which introduced some change in the CALIPSO signal. In this product (hereafter, CALIPSO–GOCCP), lidar profiles are classified into three types: clear sky profile when no cloud is detected, thin cloud profile when one or several cloud layers and a surface echo are detected, and opaque cloud profile when one or several cloud layers are detected but no surface echo is detected. Surface echo is not detected typically when the profile contains a cloud with visible optical depth > 3–5 depending on the cloud microphysical properties. The cloud base height corresponds to the lowest cloud layer detected. From this classification, five fundamental cloud properties for CRE studies are derived:

- C_{Opaque}: the opaque cloud cover, i.e. the number of opaque cloud profiles divided by the total number of profiles within a grid box.

- $Z_{T_{Opaque}}$: the altitude of opaque cloud, i.e. the average between the altitude of the highest cloud layer in the profile (Z_{Top}) and the altitude of the layer where the lidar beam is fully attenuated (Z_{FA}) is computed for each profile, a schematic illustrating these altitudes is presented in Fig. 1. Then the gridded $Z_{T_{Opaque}}$ is the average value of all the $Z_{T_{Opaque}}$ profiles within a grid box.

- C_{Thin}: the thin cloud cover, i.e. the number of thin cloud profiles divided by the total number of profiles within a grid box.

- $Z_{T_{Thin}}$: the altitude of thin cloud, i.e. the average between the altitude of the highest cloud layer in the profile (Z_{Top}) and the altitude of the lowest cloud layer (Z_{Base}) is computed for each profile, a schematic illustrating these altitudes is presented in Fig. 1. Then the gridded $Z_{T_{Thin}}$ is the average value of all the $Z_{T_{Thin}}$ profiles within a grid box.

- ε_{Thin}: the thin cloud emissivity, derived from the space lidar measurement of the thin cloud visible optical depth τ_{Thin}^{VIS} from which we estimate the thin cloud LW optical depth τ_{Thin}^{LW}, which is approximately half of τ_{Thin}^{VIS} (Garnier et al., 2015). The relationship $\varepsilon_{Thin} = 1 - e^{-\tau_{Thin}^{LW}}$ (eg. Vaillant de Guélis et al., 2017a) is computed for each profile and then averaged over all the values within a grid box.

Atmospheric
Measurement
Techniques
Discussions

Figure 1 presents the altitudes of interest of an opaque cloud and a thin cloud seen from a downward space-based lidar beam and from an upward ground-based lidar beam. A thin cloud (Fig. 1 left) is characterized by three altitudes: Z_{Top}, Z_{Base} and $Z_{T_{Thin}}$, which is the average value of the previous two ones. These three altitudes are the same when observed from a space-

115 based lidar or a ground based lidar for an ideal case.

An opaque cloud (Fig. 1 right) is characterized by three altitudes. When the lidar is based on the ground, we measure the altitude of the lowest cloud layer (Z_{Base}), the altitude where the lidar beam is fully attenuated (Z_{FA-G}), and $Z_{T_{Opaque-G}}$ which is the average of the two. When the lidar is on board a satellite, we measure the highest cloud layer (Z_{Top}), the altitude where the lidar beam is fully attenuated (Z_{FA}), and the average of the two ($Z_{T_{Opaque}}$).

120 Figure 2 illustrates the mean 2°×2° latitude-longitude gridded values of these five variables over the period 2008–2020. At global scale, opaque clouds are more numerous (42%; Fig. 2a) than thin clouds (25%; Fig. 2b) in the GOCCP v3.1.2. Note that these numbers are different from GOCCP v3.1.1 (35% and 36% respectively) where the threshold used to detect surface echo, which influences the identification of opaque clouds, was lower because GOCCP v3.1.1 (Guzman et al., 2017) was applied only to nighttime data when noise is lower than daytime. The GOCCP v3.1.2 is applied to nighttime and daytime

125 observations. As expected, the multi-year, annual mean opaque and thin cloud altitudes (Fig 2c, 2d) reach maxima (> 9 km) in the presence of deep convective clouds over the warm pool and over tropical continents, and minima (< 3 km) in subsidence regions such as over stratocumulus along the West coast of continents. The thin cloud emissivity (Fig. 2e) is larger along the ITCZ, the continental regions and around the Antarctica peninsula.

2.2 Surface LW CRE from satellites

130 In this subsection, we describe the already existing global surface LW CRE datasets derived from satellite measurements, against which we will evaluate our satellite new product.

2.2.1 CERES

(i) CERES–EBAF. The first dataset is the Clouds and the Earth's Radiant Energy System (CERES) Energy Balanced and Filled (EBAF)–Surface Ed4.0 product (Kato et al., 2013, 2018). CERES EBAF–Surface (hereafter, CERES–EBAF) is a

135 monthly mean 1°×1° gridded dataset derived from the CERES radiometers onboard the Aqua and Terra platforms. The Aqua satellite was flying in the same orbit as CALIPSO until September 2018. As CERES is a passive radiometer, CERES–EBAF is less reliable over ice surfaces and continents than over oceans. It is also less reliable in the presence of multi-layered clouds where the lower cloud may be obscured by the overlying cloud (Liu et al., 2010; Stubenrauch et al., 2013). This study uses the Edition 4.1 of the product, which differs by +0.2 W m^{-2} in global annual mean from the previous edition (Kato et al.,

140 2018).

Atmospheric
Measurement
Techniques
Open Access
EGU
Discussions

(ii) CERES–CCCM. This product combines CERES radiometer observations of TOA LW fluxes with observations from CloudSat, CALIPSO and MODIS, as well as radiative transfer calculations, to retrieve the surface LW fluxes in all sky and clear sky scenes at a resolution of the CERES Single Scanner Footprint (SSF, 20 km diameter). This product contains the

145 surface LW CRE at CERES SSF footprint and is part of the CALIPSO, CloudSat, CERES, and MODIS Merged Product (CCCM or C3M Kato et al., 2010). This product stops in 2011 because of the CloudSat battery anomaly.

2.2.2 2BFLX

The 2B–FLXHR–LIDAR P1_R04 (hereafter, 2BFLX) product is derived from combined measurements of CloudSat, CALIPSO, and the MODIS radiometer (L'Ecuyer et al., 2008; Henderson et al., 2013). It takes advantage of inferred vertical

150 profiles of cloud properties to compute surface irradiances using a broadband radiative transfer model. The dataset currently stops in 2011 when CloudSat experienced its battery anomaly. This product is sensitive to retrieval errors and biases introduced by the limited spatial and temporal characteristics of CloudSat and CALIPSO. Surface fluxes derived from a combination of radar and lidar observations in 2BFLX are also less susceptible to uncertainties due to undetected multi-layered clouds and uncertainties in cloud base height than those derived primarily from passive observations (L'Ecuyer et

155 al., 2019; Hang et al., 2019). 2BFLX surface LW CRE product (L'Ecuyer et al., 2019) is available at gridded scale as well as on instantaneous orbit file data at a resolution of the CloudSat footprint (5 km diameter).

2.3 Surface LW CRE from ground-based sites

As the retrieval of the surface CRE from space observations is not direct, we will evaluate the surface LW CRE retrieved from space against that derived from surface radiation measurements collected directly at ground-based sites. For this

160 purpose, we selected three sites located in different regions.

The first site is located in the Arctic, where constraining radiative transfer is challenging with the limited cloud, atmospheric temperature profile and humidity profile observations that are available (Kay et al., 2015) and where the surface CRE may influence the Greenland ice-cap melt (van Trich et al., 2016; Hofer et al., 2017; Shupe et al., 2013). This Summit station (Shupe et al., 2013; Gallagher et al., 2018) is located at the top of the Greenland ice cap (72.6° N–38.5° W) with an elevation

165 of 3250 m. Summit is unique because it is the only place where we have enough observations to make a robust assessment of the surface CRE over Greenland (Lacour et al., 2018). Here, the clear sky flux is computed using a radiative transfer algorithm with measurements of temperature and humidity profiles (eg., Shupe and Intrieri, 2004; Intrieri et al., 2002).

The second site is located in continental mid-latitudes. This Site Instrumental de Recherche par Télédétection Atmosphérique (SIRTA, Haeffelin et al., 2005; Chiriaco et al., 2018) is located in France (48.7° N–2.2° E) with an elevation

170 of 156 m. The data are part of the Baseline Surface Radiation Network (BSRN; Ohmura et al., 1998; Driemel et al., 2018).

Here, the clear sky flux is computed from measurements of near surface temperature and vertical distribution of humidity (Dupont et al., 2008).

The third site is located in the tropical belt where clouds influence the global climate and heat transport (Loeb et al., 2016), and where extensive deep convective clouds reach the cold tropical tropopause. Here, the surface LW CRE is small since 175 much of the surface downward LW radiation originates from emission by the moist near-surface layers of the atmosphere (Prata, 1996). This Kwajalein station (KWA, Roesch et al., 2011), which is also part of BSRN, is located in the Northern Pacific Ocean (8.72° N–167.73° E) with an elevation of 10 m.

Over the 3 ground-based sites, the radiative flux measurements at the surface are carried out using two Kipp and Zonen CM22 pyrgeometers, which measure in the spectral range of 4.5–40 µm. Observations are extracted at CALIPSO satellite 180 overpass time above these ground stations then averaged over each month.

3 Method

3.1 Approach

Vaillant de Guélis et al. (2017a; 2017b) retrieved the TOA LW CRE from the five CALIPSO–GOCCP cloud properties

185　presented in Fig. 2: the opaque cloud cover, the opaque cloud altitude, the thin cloud cover, the thin cloud altitude, and thin
cloud emissivity. In adapting their approach to the surface instead of the TOA, we developed a method to retrieve the surface
LW CRE from the same five CALIPSO–GOCCP cloud properties. Differences in physics at the surface compared to the
TOA are the followings:

3.1.1 Moisture

190　Moisture within the boundary layer influences more the surface LW CRE than the TOA LW CRE. To take moisture effects
into account, we add the surface elevation in the framework of Vaillant de Guélis et al. (2017) and we consider different
humidity and temperature profiles at a monthly resolution and every 2° in latitude, with differentiating oceans from
continents. Small variability of water vapor does not affect CRE very much compared to the fluxes themselves as the
equivalent clear sky contribution is removed from CRE. The surface LW CRE dependence on temperature and humidity

195　profiles is shown in Sect. 4.1, 4.2, and 4.3.

3.1.2 Cloud heights used for the surface LW CRE estimate

A schematic representing the cloud altitudes seen from space and ground lidars, and the radiative transfer computations
associated with each case, are represented in Figure 3.

Figure 3.A, represents an opaque cloud seen from space-based lidar (left) and the atmospheric layers that contribute to the

200　TOA LW fluxes (right). The bottom part of the cloud under Z_{FA} that is not observed by the space-based lidar does not
contribute to the TOA LW fluxes because the lidar fully attenuates typically once the lidar laser beam has penetrated through
a cloud with emissivity larger than 0.8 (eg. Vaillant de Guélis et al., 2017a)

Figure 3.B, represents an opaque cloud seen from ground-based lidar (left) and the atmospheric layers that contribute to the
surface LW fluxes (right). The top part of the cloud above Z_{FA-G} that is not observed by the ground-based lidar does not

205　contribute to the surface LW fluxes.

Figure 3.C, represents a cloud seen from space-based lidar (right) and the atmospheric layers contributing to surface LW
fluxes (downward red arrows on the right). The bottom part of the cloud under Z_{FA} that is not observed by the space-based
lidar does contribute to the surface LW fluxes.

Atmospheric
Measurement
Techniques
Discussions
Open Access
EGU

To retrieve the surface LW CRE, we could use Z_{Base} from CloudSat but this would limit our time series to 2011 only instead

210 of 2021. We chose to use what we have access to with CALIPSO: a first option consists in using Z_{FA}, the lowest opaque

cloud altitude observable by space lidar (Z_{FA}< 3 km above the surface most of the time, Guzman et al., 2017), which is

close to the actual cloud base height except in deep convective towers. A second option is to use $Z_{T_{Opaque}}$. which might

represent the altitude of emission of the cloud in some cases. This second option will overestimate the mean altitude of the

deep convective towers where the downward space-based lidar beam attenuates quickly without seeing much of the cloud

215 bottom. The bias will be larger when the cloud base temperature is far from that of Z_{FA}. Moreover, this bias will depend on

the opacity of the part of the cloud lying under Z_{FA} that is not observable by space lidar.

In our study we considered option 1 (Z_{FA}) and option 2 ($Z_{T_{Opaque}}$). For the sake of simplicity, hereafter we describe the

method with $Z_{T_{Opaque}}$ only.

3.2 Definition of the radiative quantities

220 In order to get simple notation, and because we are only interested by the CRE at the surface and in the LW domain in this

study, the surface LW CRE will be simply noted CRE in the following equations.

To infer CRE, the net LW radiative fluxes over all type of scenes (F_{Allsky}^{net}) may be compared with corresponding fluxes

where the influence of clouds has been removed ($F_{Cloudy-freesky}^{net}$). Then, we define the surface LW CRE as follow:

$$CRE = F_{Allsky}^{net} - F_{Cloudy-freesky}^{net} \qquad (1)$$

225 Using downwelling (↓) and upwelling (↑) fluxes, the surface LW CRE is expressed as follow:

$$CRE = \left(F_{Allsky}^{\downarrow} - F_{Allsky}^{\uparrow} \right) - \left(F_{Cloudy-freesky}^{\downarrow} - F_{Cloudy-freesky}^{\uparrow} \right) \qquad (2)$$

Rearranging the terms on the right-hand side of this equation, we get:

$$CRE = \left(F_{Allsky}^{\downarrow} - F_{Cloudy-freesky}^{\downarrow} \right) - \left(F_{Allsky}^{\uparrow} - F_{Cloudy-freesky}^{\uparrow} \right) \qquad (3)$$

Which can also be expressed as:

230 $$CRE = CRE^{\downarrow} - CRE^{\uparrow} \qquad (4)$$

Where $CRE^{\downarrow}$ represents the surface CRE on the LW downward fluxes and $CRE^{\uparrow}$ the surface CRE on the LW upward

fluxes. $CRE^{\uparrow}$ does not exceed 1 W m^{-2} in annual global average (Allan, 2011) and in the radiative transfer computations.

Therefore, the error in the surface properties plays a minor role.

Nevertheless, in the LW domain, clouds can warm the surface, changing the surface temperature, which is then related to the

235 upwelling LW radiation. This is a subtle but important issue and is dependent to some degree on the surface type (i.e., land

Atmospheric
Measurement
Techniques
Discussions
Open Access
EGU

surface will warm more than ocean). If CRE is determined in a hypothetical way, one could assume that the surface temperature is the same. However, this does not capture the full impact of the clouds. To understand the full impact of the clouds, one would need to consider the adjustments of all other parameters, most importantly here being the surface temperature. In this study we assume that the surface temperature is the same under clouds and clear skies, consistently with

240   the definition used in previous satellite-derived products (eg. Kato et al., 2018; L'Ecuyer et al., 2019).

Thanks to the CALIPSO–GOCCP data, it is possible to decompose the surface LW CRE into contributions due to opaque clouds and thin clouds:

$$CRE = CRE_{Opaque} + CRE_{Thin}. \qquad (5)$$

245   **3.3 Radiative transfer simulations**

We use a radiative transfer code to compute the surface LW CRE due to an opaque cloud (CRE_{Opaque}) or an optically thin cloud (CRE_{Thin}) in an atmospheric column fully overcast by that cloud. In these 1D atmospheric columns, molecules and clouds are evenly distributed within each layer and each layer is considered infinite and homogeneous. For a single column fully overcast by an opaque cloud, we establish the relationship between CRE_{Opaque} and the opaque cloud altitude $Z_{T_{Opaque}}$

250   (see Sect. 2.1). For the single column fully overcast by a thin cloud, we establish the relationship between CRE_{Thin}, the thin cloud altitude $Z_{T_{Thin}}$ (see Sect. 2.1) and the thin cloud emissivity ε_{Thin} as in Vaillant de Guélis et al. (2017)

The radiative transfer simulations are performed with GAME (Dubuisson et al., 2004). This radiative transfer code computes LW fluxes at 40 different levels with a vertical resolution of 1 km. The fluxes are spectrally integrated between 5 and 200 µm consistently with CERES measurements. We prescribe various surface temperatures and the atmospheric profiles of

255   humidity, temperature, ozone and pressure based on ERA Interim reanalysis (Dee et al., 2011) over oceans and lands for each month and latitude. Humidity and temperature profiles over land for January are presented in figure A2 in Appendix A. Figure A3 presents the seasonal and latitudinal behavior of the first layer of the humidity and temperature profiles (from the surface to 1 km above the surface) over ocean and over land. We also perform radiative transfer computations for numerous combinations of cloud opacity and vertical distribution. We prescribe the vertical extent of each cloud, the effective size of

260   cloud particles and the infrared optical thickness. For a column fully overcast by an opaque cloud, the cloud is represented by a 1 km thick cloud layer with an emissivity equal to 1 at Z_{FA-G} (Z_{Top}) above optically uniform cloud layers for different vertical extents with vertically integrated emissivity equal to 0.8. For a column fully overcast by a thin cloud, the cloud is represented by optically uniform cloud layers with vertically integrated emissivities equal to 0.1, 0.3, 0.5, or 0.7. The cloud top altitude varies according to latitude and can reach 17 km in tropical regions and only 11 km in polar regions. For

265   instance, the cloud top altitude at a latitude of 39° N takes 11 different values ranging between 2 km and 13 km, and for each

cloud top value, the cloud base altitude takes all possible values between 1 km above the surface and the cloud top altitude minus 1 km.

3.4 Retrieval of surface LW cloud radiative effect from CALIPSO observations and radiative transfer simulations

The surface LW CRE is retrieved from a theoretical expression derived from radiative transfer simulations that involves five

270 observed CALIPSO–GOCCP cloud properties (see Sect. 4). Two surface LW CRE datasets are built from CALIPSO–GOCCP observations using this theoretical relationship over the 2008–2020 period. An orbit dataset at the CALIOP footprint resolution of instantaneous cloud property observations and a 2°x2° gridded dataset of mean cloud properties. In the retrievals, we tested both Z_{FA} and $Z_{T_{Opaque}}$ for estimating the mean altitude of opaque clouds (as discussed in Sect. 3.1). An evaluation of the retrievals against independent datasets (Sect. 5) suggests that $Z_{T_{Opaque}}$ leads to retrievals that are similar

275 to other space borne retrievals while Z_{FA} leads to better agreement with ground base retrievals (Sect. 6).

4 Modeled CRE sensitivity to cloud properties

280   This section establishes parameterizations of the surface LW CRE against cloud altitude and emissivity over a single cloudy column using radiative transfer computations (Sect. 4.1). Then it analyzes the sensitivity of the surface LW CRE to the humidity and temperature profiles (Sect. 4.2), and to the surface elevation (Sect. 4.3).

4.1 Sensitivity of the CRE to cloud altitude

Figure 4 shows the results of numerous simulations for the opaque cloud column (Fig. 4a) and the thin cloud column (Fig.

285   4b) for a specific atmospheric state over oceans in January at a latitude of 39° N. CRE_{Opaque} decreases approximately linearly with opaque cloud altitude at a rate of -6 W m^{-2} km^{-1} in this atmospheric state. This figure shows that the surface LW cloud radiative effect depends mostly on the mean altitude of the cloud and only weakly on the detailed vertical cloud distribution and the cloud bottom altitude. CRE_{Thin} also decreases linearly with thin cloud altitude, and the rate of decrease depends linearly on the cloud emissivity. The linearity of these relationships is consistent with Ramanathan et al. (1977) and

290   Vaillant de Guélis et al. (2017). Based on a regression, we obtain the following linear relationships between the surface LW CRE and cloud altitude and emissivity:

$$CRE_{Opaque} = C_{Opaque} \left[a(RH,T) Z_{T_{Opaque}} + b(RH,T) \right] \tag{6}$$

$$CRE_{Thin} = C_{Thin} \left(\varepsilon_{Thin} + 0.06 \right) \left[a(RH,T) Z_{T_{Thin}} + b(RH,T) \right] \tag{7}$$

295

Where $a(RH,T)$ and $b(RH,T)$ are constants whose values depend on the humidity and temperature profiles as discussed hereafter. For the specific case presented in Fig. 4, $a = -6$ and $b = 88$.

4.2 Sensitivity of the CRE to humidity and temperature profiles

The temperature and humidity profiles in the first layers of the atmosphere largely vary according to seasons and location as

300   presented in Fig. A3 in appendix A. As these are variables that influence the surface LW CRE, their variations must be taken into account in order to retrieve the global surface LW CRE.

As an example, Figure 5.a presents the surface LW Opaque CRE for a standard humidity profile and Figure 5.b presents the surface LW Opaque CRE for an enhanced humidity profile (shown in Fig. A4). A 10% change in humidity in the first few km of the tropical atmosphere leads to a surface LW CRE change of 7.7 W m^{-2} for a cloud at 1 km and by 5 W m^{-2} for a

305   cloud at 4 km. To capture some variability of humidity and temperature, we have established similar relationships as in Fig.

Atmospheric
Measurement
Techniques
Discussions

Open Access

EGU

4 for each month and latitude (each 2°) over land and ocean. As an example, Figure A1 shows the simulations for cloud columns for an atmospheric state over land in January at a latitude of 39° N (same as Fig. 4 but over land instead of ocean).

At this latitude, the amount of humidity is lower over land than ocean, therefore the LW $F^{net}_{Cloudy-freesky}$ over land is lower and the surface LW CRE would be larger than over the ocean. The surface LW CRE is greater than that over ocean and

310 decreases with a rate ($a(RH,T)$)) of 6.5 W m^{-2} km^{-1} instead of 6 W m^{-2} km^{-1} over ocean. Figure 6 presents the latitudinal and seasonal behavior of the linear regression coefficients ($a(RH,T)$ and $b(RH,T)$). The shape of these coefficients spatio-temporal variation is influenced by the shape of the seasonal cycle of humidity and temperature in the first layers of the atmosphere (Fig. A3). For instance, the behavior of the intercept ($b(RH,T)$) over ocean and land (Fig. 6b and Fig. 6d, respectively) is driven by the shape of the humidity amount where the largest humidity amount (in tropical regions) causes

315 the smallest intercept coefficients. The seasonal cycle of the surface LW CRE is more pronounced over land than over ocean because the seasonal cycles of humidity and temperature are more pronounced over land than over ocean due to the heat capacity of the surface (Chepfer et al., 2019).

4.3 Sensitivity of the CRE to surface elevation

To take into account the surface elevation in the simulation, we consider that the surface temperature is the temperature of

320 the atmospheric layer located at the same altitude as the surface elevation with respect to sea level, and we discard all the layers located between the sea level and the surface elevation altitude. Then we performed numerous radiative transfer simulations corresponding to different clouds as described in section 3.2.

The results presented in Figure 7 show the sensitivity of the surface LW CRE to the surface elevation over continents in

January at a latitude of 39° N. As the surface elevation increases, the atmosphere is dryer so the $F^{net}_{Cloudy-freesky}$ decreases,

325 and the surface LW CRE increases. The same cloud with the same cloud properties (i.e., same altitude and emissivity) will warm a surface with a high elevation more than a low elevation. For instance, an opaque cloud at an altitude of 5.5 km msl (mean sea level) will warm a surface at sea level by 58 W m^{-2} and a surface with an elevation of 4 km msl by 102 W m^{-2}. These results are consistent with Wang et al. (2019) who found that the surface LW CRE increases over Summit station in Greenland due to the dry atmosphere at high elevations. We performed radiative transfer simulations for different surface

330 elevations at all latitudes and months (not shown) and used these to retrieve the surface LW CRE from space-based lidar observations over land. Thus, the regression coefficients over land depend in addition on surface elevation, with a 100 m resolution ($a(RH,T,SE)$, $b(RH,T,SE)$).

13

5 New CALIPSO–GOCCP surface LW cloud radiative effect

5.1 Orbit Product

Figure 8 top line shows the CALIPSO–GOCCP cloud vertical mask (Guzman et al., 2017) for two different parts of an orbit both in the tropical region. The blue areas over green areas represent the opaque clouds. The blue areas over white areas represent thin clouds. The second line represents the instantaneous surface LW CRE derived from CALIPSO–GOCCP instantaneous cloud properties (opaque cloud altitude, thin cloud altitude and emissivity; CRE_{GOCCP}) as described in Sect. 3.3. As expected, the surface LW CRE is larger for opaque clouds (Fig. 8a, ~22 W m^{-2}) than for thin clouds (Fig. 8b, ~5 W m^{-2}) for almost the same atmosphere.

5.2 Gridded Product

Figure 9a shows the map of the surface LW CRE derived from CALIPSO–GOCCP observations (CRE_{GOCCP}) over the 2008–2020 time period.

In annual global mean, clouds radiatively warm the surface in the LW domain by 27 W m^{-2}. CRE_{GOCCP} is maximal in the Southern Ocean (50–65 W m^{-2}) where the warm opaque low clouds are numerous, as already stated by L'Ecuyer et al. (2019) and Henderson et al. (2013). The north Atlantic also has particularly high values (> 55 W m^{-2}) observed between Svalbard and Greenland. In the tropics, clouds typically radiatively warm the surface in the LW domain by only 15 W m^{-2}. The moist tropical oceanic atmosphere enhances the downward clear-sky fluxes, which decreases the surface LW CRE over these ocean. The maximum tropical CRE_{GOCCP} (30 to 40 W m^{-2}) is produced by warm opaque low oceanic stratocumulus clouds along the west coast of the continents.

Over continents, the weakest CRE_{GOCCP} (< 5 W m^{-2}) occurs over Wadi Abadi basin in the Egyptian desert (25° N, 33° E), a cloud free region most of the time (80%). The largest CRE_{GOCCP} (60–65 W m^{-2}) occurs over the Tibet Autonomous Region (29° N, 97° E) where the opaque cloud cover is high (58%) and the mean surface elevation is high (4.42 km) over 2.5 million km². Here, the high amount of moisture is uplifted toward southern Tibet, amplified by Rayleigh distillation as the vapor moves over the Himalayan mountains (He et al., 2015), which enhances the formation of opaque clouds.

CALIPSO space-based lidar differentiates well opaque clouds from thin clouds. Therefore, we can decompose the surface LW CRE derived from CALIPSO–GOCCP observations into contributions due to opaque clouds (CRE_{Opaque}: Fig. 9b) and thin clouds (CRE_{Thin}: Fig 9c). This decomposition shows that 85% (23 W m^{-2}) of the overall annual global mean CRE_{GOCCP} (27 W m^{-2}) is produced by opaque clouds. Their effect is maximal (50–55 W m^{-2}) over the extra-tropical oceans (60° S and 60° N) where low warm opaque clouds are numerous. Thin clouds contribute only 15% (4 W m^{-2}) to the global

14

Atmospheric
Measurement
Techniques
Discussions

CRE_{GOCCP}, and their effect is maximal (~13 W m^{-2}) over the dry land polar regions of the Greenland and Antarctic ice sheets, where the thin cloud cover is large (~40%).

6 Evaluation of the new surface LW cloud radiative effect against independent datasets

365 **6.1 Comparison with others satellites products along piece of orbits at footprint scale**

Figure 10 shows a comparison between the surface LW CRE from the three spatial satellite retrievals along four pieces of orbits located over regions with different atmospheres and different surfaces. Figure 10 top line shows the CALIPSO–GOCCP cloud vertical mask (Guzman et al., 2017) and Figure 10 bottom line represents the comparison between the surface LW CREs.

370 Orbit A passes over the East Pacific Ocean and observes a deep convective tower, a mid-level opaque cloud at an altitude of 7 km and a low opaque cloud. The differences in surface LW CRE between the three spatial restitutions do not exceed 5 W m^{-2}. Nevertheless, within a small part of the orbit between 11.3° N and 11.8° N (Fig. B1) we observe that the CALIPSO–GOCCP retrieval is lower than the other two products because the lidar does not detect a low cloud below Z_{FA} that is detected by CloudSat (shown in Fig. B1.b)

375 Orbit B passes over the West Pacific Ocean and observes variable yet shallow clouds in the boundary layer (< 2 km). The CRE_{GOCCP} is intermittently larger than the other two products by ~15 W m^{-2}. CALIPSO–GOCCP (90 m cross track, 330 m along orbit track) detects shallow clouds in the boundary layer and, during the thickest of these, retrieves a surface LW CRE that is larger than the CERES (CloudSat) retrieval, which is based on a 20 km (5km) footprint and might miss these clouds. Orbit C passes over ocean stratocumulus regions and observes a low opaque cloud. Between 12° S and 19° S, the

380 CRE_{GOCCP} (almost 60 W m^{-2}) is smaller than CRE_{2BFLX} by ~5 W m^{-2} and smaller than CRE_{CERES} by 15 W m^{-2}. Orbit D passes over Antarctica and observes opaque clouds at high (10 km) and mid-level (4–5 km) altitudes. In the presence of high opaque clouds (between 68° S and 71° S or between 73° S and 77° S), CRE_{GOCCP} is lower than CRE_{CERES} by up to 20 W m^{-2} and CRE_{2BFLX} by up to 40 W m^{-2}, but typically compares most favourably with CRE_{CERES} over the full scene.

6.2 Global Statistical comparison with other satellites products at footprint scale over ocean

385 Figure 11a shows a comparison between the surface LW CRE from CALIPSO–GOCCP observations (90 m cross track, 330 m along orbit track) collocated with CERES–CCCM (20 km footprint) over ocean only during 2008. We consider only the CERES–CCCM footprints where all the CALIPSO–GOCCP profiles falling within this footprint are opaque and where there are more than 40 profiles. To retrieve the surface LW CRE from CALIPSO–GOCCP observations at the CERES–CCCM footprint resolutions, we average all $Z_{T_{Opaque}}$ falling within CERES–CCCM's footprint and compute the surface LW CRE

390 using the relationships found in Sect. 4.

We see a strong correlation between the surface LW CRE from CERES–CCCM observations and the surface LW CRE from CALIPSO–GOCCP observations (R=0.85). Two significant departures from the one-to-one comparison line are observed: one for high values of the surface LW CRE and the other one for low values. In the first pattern for surface LW CRE greater than 70 W m^{-2}, CRE_{GOCCP} is larger than CRE_{CERES}. This pattern corresponds to some low marine opaque clouds in mid-

395   latitude regions (not shown). To reconcile the two products, CRE_{GOCCP} should be smaller by almost 5 W m^{-2}. One way to reduce this difference would be to increase the altitudes of clouds but, due to attenuation of the signal in opaque clouds, the space-based lidar would already potentially overestimate the overall height of the clouds. Thus, the cloud height is likely not the source of this difference. Another way to reduce the surface LW CRE is by decreasing the cloud cover or the cloud opacity. However, the space-based lidar measures with precision the cloud cover thanks to its high spatial resolution and it

400   shouldn't overestimate the cloud opacity. Thus, the source of this apparent bias is more likely an underestimation of the humidity profiles used to retrieve the surface LW CRE in the presence of clouds. An increase in the humidity at these times would increase the $F^{net}_{Cloudy-freesky}$ and therefore decrease the surface LW CRE. A final possibility for the difference is that each product has a unique estimate of the cloud cover due to vastly different fields-of-view. CALIOP footprints are only a small fraction of the CERES footprint, so part of the CERES footprint could be cloud free even if the 40 CALIOP profiles

405   are opaque. A study by Kato et al. (2010) demonstrated that the differences between CERES and CloudSat/ CALIPSO cloud fractions decrease when averaged over area and time, so this difference is likely not the primary source of bias when comparing large statistical datasets.

The second regime of differences among the products is for surface LW CRE less than 30 W m^{-2} (Fig. 11a), which corresponds to high opaque clouds over the warm pool region (not shown). Here, CRE_{GOCCP} is smaller than CRE_{CERES}.

410   The underestimate of surface LW CRE by CALIPSO–GOCCP compared to CERES–CCCM could be caused by the full attenuation of the laser beam in deep convective clouds such that CALIPSO–GOCCP overestimates the mean altitude of opaque clouds.

Figure 11b represents the comparison between the surface LW CRE from CALIPSO–GOCCP observations (90 m cross track, 330 m along orbit track) collocated with CloudSat 2BFLX product at a resolution of CloudSat footprint (5 km). We

415   also consider only the CloudSat footprints where all the CALIPSO–GOCCP profiles falling within this footprint are opaque and where there are more than 10 profiles and we compute CRE_{GOCCP} by averaging all $Z_{T_{Opaque}}$ falling within CloudSat footprint.

Three significant departures from the one-to-one comparison line are observed: one for low values where CALIPSO–GOCCP < 2BFLX, one for high values of the surface LW CRE where CALIPSO–GOCCP > 2BFLX, and one for high

420   values where CALIPSO–GOCCP < 2BFLX. The two first patterns appear to be similar to Fig. 11a and show up for the same reasons as described above. The last pattern of differences among the products is for large values of CRE where 2BFLX is larger than CALIPSO–GOCCP. This pattern corresponds to a sub sample of marine opaque clouds in mid-latitude regions

(not shown) where CloudSat is able to detect lower clouds than CALIPSO. Using Z_{FA} instead of $Z_{T_{Opaque}}$ in CALIPSO–GOCCP retrieval would shift this pattern upward.

425   The differences shown in Fig. 11 are expected when comparing satellite products at footprint scales that use different remote sensing techniques. However, when looking at the gridded product distributions (fig. B4) instead of instantaneous collocated data, the 2BFLX and CALIPSO–GOCCP agree well.

6.3 Global mean comparison with other satellites products at gridded scale

Figure 12 shows global maps of differences between CALIPSO–GOCCP and the other satellite-derived products (CERES–
430   EBAF and 2BFLX). This comparison gives an overview of the differences between the three surface LW CRE spatial products but it may mask some differences given the fact that the three spatial products are averaged in time (monthly) and space (2°×2° latitude-longitude gridded).

In global annual mean, CALIPSO–GOCCP is equal compared to CERES–EBAF (CRE_{CERES}) and slightly higher compared to 2BFLX (CRE_{2BFLX} ; 0.7 W m^{-2}).

435   Compared to CERES–EBAF (Fig. 12a), CRE_{GOCCP} is larger than CRE_{CERES} over the oceans (except in stratocumulus regions) while CRE_{GOCCP} is smaller than CRE_{CERES} over icy surfaces and over ocean stratocumulus regions. The larger differences (-14 to -18 W m^{-2}) occur over Greenland, Antarctica and tropical stratocumulus regions. Over icy areas like Greenland and the Antarctic ice sheet, CERES–EBAF has limited ability to differentiate the radiative fluxes emitted by the surface from those emitted by the clouds (Liu et al., 2010; Stubenrauch et al., 2013). The retrieval of surface LW CRE with
440   CERES rely on the cloud detection from MODIS–CERES, which detects more clouds than others satellites over icy surfaces (GEWEX Cloud Assessment; Stubenrauch et al., 2012). Similarly, since stratocumulus clouds are low warm clouds at temperatures close to the surface temperature, the CERES radiometer can also have some bias when differentiating the LW cloud fluxes from LW surface fluxes over these regions.

Compared to 2BFLX (Fig. 12b), CRE_{GOCCP} is slightly larger than CRE_{2BFLX} over tropical oceans. Over lands, CRE_{GOCCP}
445   is slightly lower than CRE_{2BFLX}. The maximum difference occurs over land along the western coasts of the North and South American continents and the Himalayan mountains where the surface elevation is above 2.5 km. This difference might be due to the CloudSat CPR's long powerful pulse (Fig. B2), which generates a surface clutter echo that tends to partially mask signals from cloud forming below ~1 km (Marchand et al., 2008). Over icy polar areas, the two products are very similar.

Figure 12c shows the difference between CRE_{2BFLX} and CRE_{CERES}. The same patterns are observed over continent polar
450   regions as in Fig. 12a, where CERES–EBAF overestimates the surface LW CRE compared to the 2BFLX product.

Zonal averages of the surface LW CRE for 2008–2010 (Figure 12d) show that the surface LW CRE is generally low in tropical regions and increases towards the mid-latitudes as the atmospheric moisture decreases. Values do not vary by much

northward of about 50° N. To the south, a maximum occurs at about 60° S, with a decline towards the far south due to

declines in cloudiness. Over the broad domain reaching from 60° N to 60° S the three satellites techniques show similar

455   zonal means with differences among the three typically not exceeding 3 W m^{-2}. Over polar regions, the surface LW CRE

from CERES–EBAF is generally higher than the other two products derived from active sensors.

6.4 Comparison with ground-based stations at gridded scale

Comparisons between ground-based measurements and the satellite-derived products (CRE_{GOCCP}, CRE_{CERES}, CRE_{2BFLX})

provide a direct evaluation of the satellite retrievals, but are limited by the difference in the spatial resolution of the satellite-

460   derived product (2°×2°) and the ground station observations (a few meters). The locations of the three ground-based sites are

reported in the maps (stars in Fig. 12c).

Over the Summit Station, Greenland site, on average compared to ground-based observations, CALIPSO–GOCCP

underestimates the surface LW CRE by 8.5 W m^{-2}, while 2BFLX underestimates it by 16.4 W m^{-2} and CERES–EBAF

overestimates it by 36.6 W m^{-2} (Fig. 13a). The comparison of averages is made only when all products are available and for

465   the Greenland site, this is just for three months (JFM 2011). Averages over the 2008–2011 and 2011–2016 periods (Fig. 14)

show that these biases calculated for a short period are similar to the longer periods. Over the 2008–2011 time period,

CRE_{GOCCP} is close to CRE_{2BFLX} and both show consistent summer maxima and winter minima. CRE_{CERES} follows a

different annual cycle with maxima wider and shifted by about two to six months. Over the 2011–2016 time period,

CRE_{GOCCP} and the ground station data show similar annual cycles, while the CRE_{CERES} annual cycle continues to be

470   shifted by two to four month and generally has different annual variability compared to ground station. The same behavior

where CERES–EBAF overestimates the surface LW CRE comparing to CALIPSO–GOCCP is observed over the map of

difference (Fig. 12a) in icy polar regions, for instance over Greenland and Antarctica ice sheet. While this comparison

suggests that CALIPSO–GOCCP could be biased somewhat low compared to the ground-station perspective over

Greenland, it is also clear that this approach does appropriately capture the annual variability, while the CERES–EBAF

475   approach appears to be significantly biased high with an unrealistic annual cycle.

Over the mid-latitude continental site (Fig. 13b) on average, CALIPSO–GOCCP underestimates the surface LW CRE by 5.7

W m^{-2} compared to ground-based observations, while 2BFLX underestimates it by 9.4 W m^{-2} and CERES–EBAF

underestimates it by 12.1 W m^{-2}.

Over the tropical ocean site (Fig. 13c) on average, CALIPSO–GOCCP underestimates the surface LW CRE by 2.3 W m^{-2}

480   compared to ground-based observations, while CERES–EBAF underestimates it by 2.7 W m^{-2} and 2BFLX underestimates it

by 4.1 W m^{-2}. This same behavior is found on the map of differences between CRE_{GOCCP} and CRE_{2BFLX} (Fig. 12b) along

the tropical Pacific and tropical Atlantic oceans where 2BFLX underestimates the surface LW CRE comparing to

CALIPSO–GOCCP.

Atmospheric
Measurement
Techniques
Open Access
Discussions
EGU

6.5 Space lidar missing the opaque cloud base

485   CALIPSO does not see the cloud base in many stratiform-type clouds, as an example, but this does not lead to as big of an issue in the surface LW CRE retrieval because the stratiform cloud base is not very far from the point of attenuation of the lidar. On the other hand, this attenuation can become a significant issue for circumstances where the lidar signal is fully attenuated at an altitude that is significantly above the actual cloud base, such as in deep convective clouds.

Based on the comparison of orbits (Fig. B1), we observe that when the space lidar does not see the cloud base, CALIPSO
490   LW CRE underestimates the local surface LW CRE compared to 2BFLX. However, the opaque deep convective clouds cover a small part of the overall tropics compared to others clouds, therefore this effect does not dominate the global comparison (Fig. 12) where CALIPSO–GOCCP surface LW CRE, is on the contrary, slightly larger than the other satellite products.

To test if the differences between CALIPSO–GOCCP and other products come from the space lidar not seeing the cloud
495   base, we used Z_{FA} instead of $Z_{T_{Opaque}}$ in the CALIPSO–GOCCP retrieval. By definition Z_{FA} is always lower in altitude than $Z_{T_{Opaque}}$, therefore this change should reduce the difference between the CALIPSO–GOCCP surface LW CRE and other surface LW CREs if the differences were due to CALIPSO missing the cloud base. Fig. B3 shows that the difference between CALIPSO–GOCCP surface LW CRE and the other satellite products increases instead of reduces when using Z_{FA} instead of $Z_{T_{Opaque}}$. This suggests that the differences in surface LW CRE are likely not often due to CALIPSO mis-
500   representing the cloud base and that the cloud base might not be far from $Z_{T_{Opaque}}$ in the majority of the cases. This result also suggests that the differences between the satellite retrievals come from other sources, such as the assumed humidity and temperature profiles. Indeed, the resolution of these profiles is rough in the CALIPSO retrieval and these profiles have also been identified as the largest sources of LW flux uncertainty in the 2BFLX product (Henderson et al., 2013).

Nevertheless contrarily to the satellite retrieval inter-comparison, using Z_{FA} instead of $Z_{T_{Opaque}}$ leads to slightly better
505   agreement of CALIPSO–GOCCP LW CRE with ground base retrievals (eg. Fig. 13, 14). Ground-based measurements derive directly the surface LW CRE. While there are certainly challenges in comparing ground-based and satellite estimates, we should consider the ground-based estimates to be of pretty high quality. Thus, what these results mean collectively is that: 1)The inability of CALIPSO to observe the cloud base likely does have some effect (with respect to ground-based measurements). And that 2) this effect actually makes the comparison with other satellite products worse, which means that
510   there are other issues (possibly with the other satellite products) leading to further differences.

7 Variation of the Surface LW CRE

7.1 Seasonal variation

7.1.1 Over ground base sites

Figure 14 presents the comparison of seasonal cycles between the satellite retrievals and the ground-based observations.
515 Over the Greenland site (Fig. 14a,d), CALIPSO–GOCCP and 2BFLX find the same seasonal cycle of the surface LW CRE with maxima in July, that correspond to the maximum opaque cloud cover, same as the ground-based seasonal cycle. The CERES–EBAF retrieval maximum is shifted by about three months (October, Fig. 14a,d), to a time of year that shows the minimum opaque cloud cover based on CALIPSO–GOCCP (not shown). This result suggests that during these months the CERES–EBAF retrieval does not successfully distinguish LW upward fluxes from clouds and the surface. This is consistent
520 with CERES–EBAF low-mid and high-mid cloud fractions being biased high over the Summit site except for summer time (not shown). Consistently, Figure 14d shows CERES–EBAF's surface LW CRE is overestimated compared to ground-base retrievals in all season except summer. As a consequence CERES–EBAF does not capture the surface LW CRE annual cycle, contrarily to CALIPSO–GOCCP and 2BFLX retrievals.

Over the mid-latitude continental site (Fig. 14b,e), the surface LW CRE seasonal cycle of CALIPSO–GOCCP and 2BFLX
525 are close to each other and the three satellite-derived products show similar seasonal cycles as the ground station.

Over the tropical ocean site (Fig. 14c,f), the surface LW CRE seasonal cycle is relatively flat.

7.1.2 Global mean (2008–2020)

Figure 15a represents the global average seasonal cycle of the three surface LW CRE satellite-derived products. CRE_{CERES} is larger than CRE_{GOCCP} and CRE_{2BFLX} from October to February and is lower from May to September. To analyze these
530 differences, we decomposed the globe into Northern Hemisphere (NH : Fig. 15b), NH–ocean (Fig. 15c), NH–land (Fig. 15d), and Southern Hemisphere (SH : Fig. 15e), SH–ocean (Fig. 15f), SH–land (Fig. 15g).

The NH winter is the main cause for CERES–EBAF being larger than the two other products from October to February (2–3 W m^{-2}). The NH–continents have the largest contribution (~6 W m^{-2}) and the NH–oceans contribute slightly (~1 W m^{-2}) between January to March which corresponds to the maximum of sea ice (Rousset et al., 2015). The SH only contributes a
535 little (~0.5 W m^{-2}) for the months of October and November and this comes only from the Antarctic ice sheet, which is covered by ice all year long. Same as in the difference maps (Fig. 12a), MODIS–CERES detects more clouds than other satellites over icy surfaces (GEWEX Cloud Assessment ; Stubenrauch et al., 2012).

The lower CERES–EBAF compared to CALIPSO–GOCCP and 2BFLX (1–2 W m^{-2}) from May to September is mostly caused by both the oceans in SH and the land in NH.

Atmospheric
Measurement
Techniques
Discussions

Open Access

EGU

7.1.3 Seasonal evolution of the zonal mean

Figure 16 represents the annual evolution of the zonal mean of the surface LW CRE from CERES–EBAF (Fig. 16a), CALIPSO–GOCCP (Fig. 16b), and 2BFLX (Fig. 16c). The two active sensor figures exhibit the same behavior whilst CERES–EBAF has a stronger surface LW CRE in the polar regions during winter months, which corresponds to the minimum of opaque cloud cover and the maximum of sea ice. To see where the largest differences with CERES–EBAF are located, Figures 16d and 16e represent the differences between CALIPSO–GOCCP and CERES–EBAF and the differences between 2BFLX and CERES–EBAF respectively. The same feature is observed in both figures with CERES–EBAF having larger surface LW CRE than the other two products in the polar regions during their respective winters. CERES–EBAF also has smaller surface LW CRE in the mid-latitude regions.

Decomposing the difference (Fig. 16d) into land only (Fig. 16f) and ocean only (Fig. 16g) shows CALIPSO–GOCCP lower than CERES–EBAF over NH land [50° N to 80° N] during winter (September to May) and over the icy Antarctic all year long. The oceans contribute to this difference during months of significant sea ice. These results suggests that the differences in surface LW CRE are likely due to CERES–EBAF detecting clouds over icy surfaces when there are no clouds (Stubenrauch et al., 2012).

On the contrary, CERES–EBAF is lower than CALIPSO–GOCCP mostly over mid-latitude oceanic regions all year long (Fig. 16g) and this difference is also observed in the annual mean maps (Fig 12a). These regions contain low altitude thin clouds and few low opaque clouds (1–2 km: Fig. 2b,d). To see if these differences are caused by thin clouds in the boundary layer, we have computed the difference between the surface LW opaque CRE from CALIPSO–GOCCP observations and the CERES–EBAF product (Fig. 16h) over ocean only. The differences over mid-latitude oceans are smaller and close to 0 in this case (Fig. 16h). Thus, the reason for the CERES–EBAF surface LW CRE being weaker than the CALIPSO–GOCCP in these regions is likely because the CERES radiometer does not see the optically thin clouds in the boundary layer over mid-latitude oceans.

7.2 Variations of 13 years (2008–2020)

Figure 17a shows the temporal evolution of the surface LW CRE anomaly from the three satellite-derived products over 13 years 2008–2020. A decomposition separating continents from oceans and NH from SH is presented in Figs. 17b–*g*.

There is consistent amplitude in the annual variability in the global surface LW CRE anomaly between the three datasets. This appears to be because of the annual cycle variations in the SH and NH, which are out of sync from each other, and the fact that the SH annual amplitude (and magnitude) are larger. Thus, the annual variation of the global surface LW CRE is most closely aligned with the annual variation of the SH.

The phasing of the annual cycle of CRE_{GOCCP} and CRE_{2BFLX} anomalies are roughly similar over the 2008–2010 time period while, as noted before, the CRE_{CERES} anomaly shows a shift in the annual cycle of about two months compared to

Atmospheric
Measurement
Techniques
Discussions

Open Access

EGU

the other two satellite-derived products. This shift remains between CRE_{CERES} and CRE_{GOCCP} anomalies over the 13 years. The phasing of the annual cycle for the CERES–EBAF product is actually quite consistent with the others for both NH and SH over both land and ocean, except for the NH land (Fig. 17d; because of false cloud detection as already explained and shown in Figs. 14–16). However, it is interesting that even over NH land the annual minima match pretty well. Thus, the

575   overall two months shift (Fig. 17a) is in part due to the differences in NH land annual maximum but apparently also somewhat due to the different amplitudes of the annual cycles for different areas and how they combine in unique ways for the different datasets.

The inter-annual variability is pretty interesting. For example, the NH winter max in CERES–EBAF and CALIPSO–GOCCP products appears to vary by up to about 3 W m^{-2} from year to year. That is the kind of variability that might have significant

580   impacts on climate-relevant processes like melting of the cryosphere.

Atmospheric
Measurement
Techniques
Discussions

8 Conclusion

In this paper, we build a new surface LW CRE dataset from five cloud properties observed with space-based lidar (CALIPSO–GOCCP). The robustness of the new surface LW CRE dataset at global scales is evaluated by comparing it

585   against existing independent space-based surface LW CRE retrievals from CERES and CloudSat (Kato et al., 2018; L'Ecuyer et al., 2019) at footprint instantaneous scale as well as at 2°x2° gridded scale globally. It is also evaluated locally by comparison against observations collected at three ground stations in polar (Shupe et al., 2013), mid-latitude (Haeffelin et al., 2005; Chiriaco et al., 2018) and tropical (Roesch et al., 2011) locations. The (admittedly limited) ground-station comparisons actually showed that the CALIPSO–GOCCP product agreed the best with the ground measurements compared

590   to the other satellite products, especially in capturing the annual variability. Additionally, there are other specific aspects where the CALIPSO–GOCCP product appears to be an improvement over others, including over bright polar surfaces.

This might be surprising given the simplicity of the surface radiation retrieval method used to produce the CALIPSO–GOCCP product, but it is understandable because of the two following physical elements:

i) The CALIPSO–GOCCP method directly retrieves the surface LW CRE without retrieving the surface radiative fluxes first.

595   This approach minimizes the impact of the uncertainties due to surface characteristics (surface emissivity, roughness, deserts and frozen surfaces), which strongly influence the fluxes but not the surface LW CRE.

ii) The surface LW CRE is primarily driven by the cloud cover, the cloud opacity and the cloud altitude, which are quite well measured by space-based lidar over all types of surfaces. Moreover, the lidar approach distinguishes quite well the opaque clouds from the optically thin clouds. Lastly, it documents the detailed vertical cloud profile, except below the altitude where

600   the laser is fully attenuated where we overestimate the mean altitude of opaque clouds. This last limitation only weakly influences the surface LW CRE retrieval because the lidar is fully attenuated at an altitude lower than 3 km above the surface most of the time (Guzman et al., 2017) except in deep convection and some mid-latitude clouds. Indeed, along deep convective tropical regions where the attenuation of the lidar beam might not see the whole bottom part of the cloud and can underestimate the surface LW CRE by almost 5 W m^{-2}. All three satellite datasets exhibit some differences relative to

605   ground-based measurements.

The evaluation of this new CALIPSO based surface LW CRE against other datasets also showed that overall this new retrieval agrees well with CloudSat-based estimate (L'Ecuyer et al., 2019) but this latter is limited in time until only 2011 due to a battery anomaly. Compared to CERES–EBAF, the new CALIPSO–GOCCP based dataset provides new and more reliable information on the surface LW CRE over specific regions such as over icy and continental regions, where space-

610   based lidar is successful in distinguishing clouds from the surface, and over mid-latitude oceans, where space-lidar detects well optically thin small clouds.

This new global dataset extends over more than a decade thanks to the long CALIPSO mission. The global mean temporal evolution over 13 years (2008–2020) shows that the anomaly of the surface LW CRE derived from CALIPSO–GOCCP is shifted by about two months compared to that derived from the passive CERES radiometer. This shift is mostly due to

615 differences over the NH lands during winter when the surface is icy. This new dataset will be extended in time by including future data acquired by CALIPSO, as well as with data collected by forthcoming space lidars on board the European Earth Cloud, Aerosol and Radiation Explorer mission (EarthCARE; Illingworth et al., 2015) and the next generation of US cloud/aerosols lidar space missions.

The dataset presented in this paper will be used in a future study to better understand the mechanisms of cloud radiative

620 feedbacks at the Earth's surface, i.e. how a change in surface temperature modifies the cloud properties that change the surface LW CRE, which in turn influences the temperature. An essential first step is to understand which cloud variables have driven the surface LW CRE variations over the last decade in regions that are most sensitive to global warming, such as the polar regions, as well as on a global scale. Several recent studies (eg. Taylor et al., 2007; Zelinka et al., 2012a, 2012b ; Vaillant de Guélis et al., 2017a, 2017b, 2018) have shown that it is possible to attribute changes in CRE to variations in

625 cloud properties when 1) the CRE is related to a limited number of cloud properties by sufficiently simple relationships that they can be derived analytically, 2) the CRE retrieved by these analytical relationships is sufficiently reliable, i.e. within the uncertainty domain of the existing datasets, and 3) the CRE is retrieved using reliable observations over all surface types and on long global time scale. The CALIPSO–GOCCP surface LW CRE dataset developed in this study satisfies these three conditions. The next step of this work will therefore be to analyze this 13 years dataset to understand these mechanisms. The

630 goal of this research is to improve our understanding of the response of clouds to the warming induced by anthropogenic activities, which is a major source of uncertainty in climate change predictions.

Data: the new CALIPSO–GOCCP surface LW CRE dataset presented in this paper will be made available on

640 https://climserv.ipsl.polytechnique.fr/cfmip-obs/index.html

Appendix A: Sensitivity of the surface LW CRE to humidity and temperature

Appendix B: Sensitivity of the surface LW CRE to cloud base height

References

Acquaotta, F. and Fratianni, S.: THE IMPORTANCE OF THE QUALITY AND RELIABILITY OF THE HISTORICAL
645   TIME SERIES FOR THE STUDY OF CLIMATE CHANGE, ABClima, 14, https://doi.org/10.5380/abclima.v14i1.38168,
2014.

Allan, R. P.: Combining satellite data and models to estimate cloud radiative effect at the surface and in the atmosphere:
Cloud radiative effect at the surface and in the atmosphere, Met. Apps, 18, 324–333, https://doi.org/10.1002/met.285, 2011.

van den Broeke, M., Bamber, J., Ettema, J., Rignot, E., Schrama, E., van de Berg, W. J., van Meijgaard, E., Velicogna, I.,
650   and   Wouters,   B.:   Partitioning   Recent   Greenland   Mass   Loss,   Science,   326,   984–986,
https://doi.org/10.1126/science.1178176, 2009.

Cesana, G., Kay, J. E., Chepfer, H., English, J. M., and Boer, G.: Ubiquitous low level liquid containing Arctic clouds:
New observations and climate model constraints from CALIPSO GOCCP, Geophys. Res. Lett., 39, 2012GL053385, https://
doi.org/10.1029/2012GL053385, 2012.

655   Chepfer, H., Bony, S., Winker, D., Cesana, G., Dufresne, J. L., Minnis, P., Stubenrauch, C. J., and Zeng, S.: The GCM-
Oriented   CALIPSO   Cloud   Product   (CALIPSO–GOCCP),   J.   Geophys.   Res.,   115,   D00H16,
https://doi.org/10.1029/2009JD012251, 2010.

Chepfer, H., Brogniez, H., and Noel, V.: Diurnal variations of cloud and relative humidity profiles across the tropics, Sci
Rep, 9, 16045, https://doi.org/10.1038/s41598-019-52437-6, 2019.

660   Chiriaco, M., Dupont, J.-C., Bastin, S., Badosa, J., Lopez, J., Haeffelin, M., Chepfer, H., and Guzman, R.: ReOBS: a new
approach to synthesize long-term multi-variable dataset and application to the SIRTA supersite, Earth Syst. Sci. Data, 10,
919–940, https://doi.org/10.5194/essd-10-919-2018, 2018.

Chylek, P., Lohmann, U., Dubey, M., Mishchenko, M., Kahn, R., and Ohmura, A.: Limits on climate sensitivity derived
from recent satellite and surface observations, J. Geophys. Res., 112, D24S04, https://doi.org/10.1029/2007JD008740, 2007.

665   Curry, J. A., Schramm, J. L., Rossow, W. B., and Randall, D.: Overview of Arctic cloud and radiation characteristics, 9,
1731–1764, 1996.

Dee, D. P., Uppala, S. M., Simmons, A. J., Berrisford, P., Poli, P., Kobayashi, S., Andrae, U., Balmaseda, M. A., Balsamo,
G., Bauer, P., Bechtold, P., Beljaars, A. C. M., van de Berg, L., Bidlot, J., Bormann, N., Delsol, C., Dragani, R., Fuentes, M.,
Geer, A. J., Haimberger, L., Healy, S. B., Hersbach, H., Hólm, E. V., Isaksen, L., Kållberg, P., Köhler, M., Matricardi, M.,
670   McNally, A. P., Monge-Sanz, B. M., Morcrette, J.-J., Park, B.-K., Peubey, C., de Rosnay, P., Tavolato, C., Thépaut, J.-N.,
and Vitart, F.: The ERA-Interim reanalysis: configuration and performance of the data assimilation system, Q.J.R. Meteorol.
Soc., 137, 553–597, https://doi.org/10.1002/qj.828, 2011.

Driemel, A., Augustine, J., Behrens, K., Colle, S., Cox, C., Cuevas-Agulló, E., Denn, F. M., Duprat, T., Fukuda, M., Grobe,
H., Haeffelin, M., Hodges, G., Hyett, N., Ijima, O., Kallis, A., Knap, W., Kustov, V., Long, C. N., Longenecker, D., Lupi,
675   A., Maturilli, M., Mimouni, M., Ntsangwane, L., Ogihara, H., Olano, X., Olefs, M., Omori, M., Passamani, L., Pereira, E.
B., Schmithüsen, H., Schumacher, S., Sieger, R., Tamlyn, J., Vogt, R., Vuilleumier, L., Xia, X., Ohmura, A., and König-

Langlo, G.: Baseline Surface Radiation Network (BSRN): structure and data description (1992–2017), Earth Syst. Sci. Data, 10, 1491–1501, https://doi.org/10.5194/essd-10-1491-2018, 2018.

Dubuisson, P.: Water vapor retrieval over ocean using near-infrared radiometry, J. Geophys. Res., 109, D19106, https://doi.org/10.1029/2004JD004516, 2004.

Dupont, J.-C. and Haeffelin, M.: Observed instantaneous cirrus radiative effect on surface-level shortwave and longwave irradiances, J. Geophys. Res., 113, D21202, https://doi.org/10.1029/2008JD009838, 2008.

Gallagher, M. R., Shupe, M. D., and Miller, N. B.: Impact of Atmospheric Circulation on Temperature, Clouds, and Radiation at Summit Station, Greenland, with Self-Organizing Maps, J. Climate, 31, 8895–8915, https://doi.org/10.1175/JCLI-D-17-0893.1, 2018.

Garnier, A., Pelon, J., Vaughan, M. A., Winker, D. M., Trepte, C. R., and Dubuisson, P.: Lidar multiple scattering factors inferred from CALIPSO lidar and IIR retrievals of semi-transparent cirrus cloud optical depths over oceans, Atmos. Meas. Tech., 8, 2759–2774, https://doi.org/10.5194/amt-8-2759-2015, 2015.

Guzman, R., Chepfer, H., Noel, V., Vaillant de Guélis, T., Kay, J. E., Raberanto, P., Cesana, G., Vaughan, M. A., and Winker, D. M.: Direct atmosphere opacity observations from CALIPSO provide new constraints on cloud-radiation interactions: GOCCP v3.0 OPAQ Algorithm, J. Geophys. Res. Atmos., 122, 1066–1085, https://doi.org/10.1002/2016JD025946, 2017.

Haeffelin, M., Barthès, L., Bock, O., Boitel, C., Bony, S., Bouniol, D., Chepfer, H., Chiriaco, M., Cuesta, J., Delanoë, J., Drobinski, P., Dufresne, J.-L., Flamant, C., Grall, M., Hodzic, A., Hourdin, F., Lapouge, F., Lemaître, Y., Mathieu, A., Morille, Y., Naud, C., Noël, V., O'Hirok, W., Pelon, J., Pietras, C., Protat, A., Romand, B., Scialom, G., and Vautard, R.: SIRTA, a ground-based atmospheric observatory for cloud and aerosol research, Ann. Geophys., 23, 253–275, https://doi.org/10.5194/angeo-23-253-2005, 2005.

Hang, Y., L'Ecuyer, T. S., Henderson, D. S., Matus, A. V., and Wang, Z.: Reassessing the Effect of Cloud Type on Earth's Energy Balance in the Age of Active Spaceborne Observations. Part II: Atmospheric Heating, 32, 6219–6236, https://doi.org/10.1175/JCLI-D-18-0754.1, 2019.

He, Y., Risi, C., Gao, J., Masson-Delmotte, V., Yao, T., Lai, C.-T., Ding, Y., Worden, J., Frankenberg, C., Chepfer, H., and Cesana, G.: Impact of atmospheric convection on south Tibet summer precipitation isotopologue composition using a combination of in situ measurements, satellite data, and atmospheric general circulation modeling: IMPACT OF CONVECTION ON TP ISOTOPIC, J. Geophys. Res. Atmos., 120, 3852–3871, https://doi.org/10.1002/2014JD022180, 2015.

Henderson, D. S., L'Ecuyer, T., Stephens, G., Partain, P., and Sekiguchi, M.: A Multisensor Perspective on the Radiative Impacts of Clouds and Aerosols, 52, 853–871, https://doi.org/10.1175/JAMC-D-12-025.1, 2013.

Hofer, S., Tedstone, A. J., Fettweis, X., and Bamber, J. L.: Decreasing cloud cover drives the recent mass loss on the Greenland Ice Sheet, 9, 2017.

Illingworth, A. J., Barker, H. W., Beljaars, A., Ceccaldi, M., Chepfer, H., Clerbaux, N., Cole, J., Delanoë, J., Domenech, C., Donovan, D. P., Fukuda, S., Hirakata, M., Hogan, R. J., Huenerbein, A., Kollias, P., Kubota, T., Nakajima, T., Nakajima, T. Y., Nishizawa, T., Ohno, Y., Okamoto, H., Oki, R., Sato, K., Satoh, M., Shephard, M. W., Velázquez-Blázquez, A., Wandinger, U., Wehr, T., and Zadelhoff, G.-J. van: The EarthCARE Satellite: The Next Step Forward in Global

Atmospheric
Measurement
Techniques
Discussions

Open Access
EGU

Measurements of Clouds, Aerosols, Precipitation, and Radiation, 96, 1311–1332, https://doi.org/10.1175/BAMS-D-12-00227.1, 2015.

Intrieri, J. M., Fairall, C. F., Shupe, M. D., Persson, P. O. G., Andreas, E. L., Guest, P., Moritz, R. M.: An annual cycle of Arctic surface cloud forcing at SHEBA, J. Geophys. Res., 107, 8039, https://doi.org/10.1029/2000JC000439, 2002.

IPCC, (2021). Climate Change 2021: The Physical Science Basis. Contribution of Working Group I to the Sixth Assessment Report of the Intergovernmental Panel on Climate Change, in: Masson-Delmotte, V., Zhai, P., Pirani, A., Connors, S., L, Péan, C., Berger, S., Caud, N., Chen, Y., Goldfarb, L., Gomis, M., I, Huang, M., Leitzell, K., Lonnoy, E., Matthews, J., B, R, Maycock, T., K, Waterfield, T., Yelekçi, O., Yu, R., Zhou, B. (Eds.), Cambridge University Press. In Press.

Kato, S., Rose, F. G., Rutan, D. A., and Charlock, T. P.: Cloud Effects on the Meridional Atmospheric Energy Budget Estimated from Clouds and the Earth's Radiant Energy System (CERES) Data, 21, 4223–4241, https://doi.org/10.1175/2008JCLI1982.1, 2008.

Kato, S., Sun-Mack, S., Miller, W. F., Rose, F. G., Chen, Y., Minnis, P., and Wielicki, B. A.: Relationships among cloud occurrence frequency, overlap, and effective thickness derived from CALIPSO and CloudSat merged cloud vertical profiles, J. Geophys. Res., 115, D00H28, https://doi.org/10.1029/2009JD012277, 2010.

Kato, S., Loeb, N. G., Rose, F. G., Doelling, D. R., Rutan, D. A., Caldwell, T. E., Yu, L., and Weller, R. A.: Surface Irradiances Consistent with CERES-Derived Top-of-Atmosphere Shortwave and Longwave Irradiances, 26, 2719–2740, https://doi.org/10.1175/JCLI-D-12-00436.1, 2013.

Kato, S., Rose, F. G., Rutan, D. A., Thorsen, T. J., Loeb, N. G., Doelling, D. R., Huang, X., Smith, W. L., Su, W., and Ham, S.-H.: Surface Irradiances of Edition 4.0 Clouds and the Earth's Radiant Energy System (CERES) Energy Balanced and Filled (EBAF) Data Product, 31, 4501–4527, https://doi.org/10.1175/JCLI-D-17-0523.1, 2018.

Kay, J. E., Hillman, B. R., Klein, S. A., Zhang, Y., Medeiros, B., Pincus, R., Gettelman, A., Eaton, B., Boyle, J., Marchand, R., and Ackerman, T. P.: Exposing Global Cloud Biases in the Community Atmosphere Model (CAM) Using Satellite Observations and Their Corresponding Instrument Simulators, 25, 5190–5207, https://doi.org/10.1175/JCLI-D-11-00469.1, 2012.

Kay, J. E., Deser, C., Phillips, A., Mai, A., Hannay, C., Strand, G., Arblaster, J. M., Bates, S. C., Danabasoglu, G., Edwards, J., Holland, M., Kushner, P., Lamarque, J.-F., Lawrence, D., Lindsay, K., Middleton, A., Munoz, E., Neale, R., Oleson, K., Polvani, L., and Vertenstein, M.: The Community Earth System Model (CESM) Large Ensemble Project: A Community Resource for Studying Climate Change in the Presence of Internal Climate Variability, 96, 1333–1349, https://doi.org/10.1175/BAMS-D-13-00255.1, 2015.

King, J. C., Gadian, A., Kirchgaessner, A., Kuipers Munneke, P., Lachlan-Cope, T. A., Orr, A., Reijmer, C., van den Broeke, M. R., van Wessem, J. M., and Weeks, M.: Validation of the summertime surface energy budget of Larsen C Ice Shelf (Antarctica) as represented in three high-resolution atmospheric models: Surface energy budget of Larsen C, J. Geophys. Res. Atmos., 120, 1335–1347, https://doi.org/10.1002/2014JD022604, 2015.

Kopp, R. E., Kemp, A. C., Bittermann, K., Horton, B. P., Donnelly, J. P., Gehrels, W. R., Hay, C. C., Mitrovica, J. X., Morrow, E. D., and Rahmstorf, S.: Temperature-driven global sea-level variability in the Common Era, Proc Natl Acad Sci USA, 113, E1434–E1441, https://doi.org/10.1073/pnas.1517056113, 2016.

750 Kwok, R. and Untersteiner, N.: The thinning of Arctic sea ice, Physics Today, 64, 36–41, https://doi.org/10.1063/1.3580491, 2011.

Lacour, A., Chepfer, H., Miller, N. B., Shupe, M. D., Noel, V., Fettweis, X., Gallee, H., Kay, J. E., Guzman, R., and Cole, J.: How Well Are Clouds Simulated over Greenland in Climate Models? Consequences for the Surface Cloud Radiative Effect over the Ice Sheet, J. Climate, 31, 9293–9312, https://doi.org/10.1175/JCLI-D-18-0023.1, 2018.

755 L'Ecuyer, T. S., Wood, N. B., Haladay, T., Stephens, G. L., and Stackhouse, P. W.: Impact of clouds on atmospheric heating based on the R04 CloudSat fluxes and heating rates data set, J. Geophys. Res., 113, D00A15, https://doi.org/10.1029/2008JD009951, 2008.

L'Ecuyer, T. S., Hang, Y., Matus, A. V., and Wang, Z.: Reassessing the Effect of Cloud Type on Earth's Energy Balance in the Age of Active Spaceborne Observations. Part I: Top of Atmosphere and Surface, 32, 6197–6217, https://doi.org/10.1175/ 760 JCLI-D-18-0753.1, 2019.

Lindzen, R. S. and Choi, Y.-S.: The Iris Effect: A Review, Asia-Pacific J Atmos Sci, https://doi.org/10.1007/s13143-021-00238-1, 2021.

Liu, Y., Ackerman, S. A., Maddux, B. C., Key, J. R., and Frey, R. A.: Errors in Cloud Detection over the Arctic Using a Satellite Imager and Implications for Observing Feedback Mechanisms, 23, 1894–1907, 765 https://doi.org/10.1175/2009JCLI3386.1, 2010.

Loeb, N. G., Wang, H., Cheng, A., Kato, S., Fasullo, J. T., Xu, K.-M., and Allan, R. P.: Observational constraints on atmospheric and oceanic cross-equatorial heat transports: revisiting the precipitation asymmetry problem in climate models, Clim Dyn, 46, 3239–3257, https://doi.org/10.1007/s00382-015-2766-z, 2016.

Norris, J. R., Allen, R. J., Evan, A. T., Zelinka, M. D., O'Dell, C. W., and Klein, S. A.: Evidence for climate change in the 770 satellite cloud record, Nature, 536, 72–75, https://doi.org/10.1038/nature18273, 2016.

Ohmura, A., Dutton, E. G., Forgan, B., Fröhlich, C., Gilgen, H., Hegner, H., Heimo, A., König-Langlo, G., McArthur, B., and Müller, G.: Baseline Surface Radiation Network (BSRN/WCRP): New precision radiometry for climate research, 79, 2115–2136, 1998.

Prata, A. J.: A new long-wave formula for estimating downward clear-sky radiation at the surface, Q.J Royal Met. Soc., 122, 775 1127–1151, https://doi.org/10.1002/qj.49712253306, 1996.

Ramanathan, V.: Interactions between ice-albedo, lapse-rate and cloud-top feedbacks: An analysis of the nonlinear response of a GCM climate model, 34, 1885–1897, 1977.

Ramanathan, V., Cess, R. D., Harrison, E. F., Minnis, P., and Barkstrom, B. R.: Cloud-Radiative Forcing and Climate: Results from te Earth Radiation Budget Experiment, 243, 8, 1989.

780 Roesch, A., Wild, M., Ohmura, A., Dutton, E. G., Long, C. N., and Zhang, T.: Assessment of BSRN radiation records for the computation of monthly means, Atmos. Meas. Tech., 4, 339–354, https://doi.org/10.5194/amt-4-339-2011, 2011.

Rousset, C., Vancoppenolle, M., Madec, G., Fichefet, T., Flavoni, S., Barthélemy, A., Benshila, R., Chanut, J., Levy, C., Masson, S., and Vivier, F.: The Louvain-La-Neuve sea ice model LIM3.6: global and regional capabilities, Geosci. Model Dev., 8, 2991–3005, https://doi.org/10.5194/gmd-8-2991-2015, 2015.

785 Scott, R. C., Lubin, D., Vogelmann, A. M., and Kato, S.: West Antarctic Ice Sheet Cloud Cover and Surface Radiation Budget from NASA A-Train Satellites, J. Climate, 30, 6151–6170, https://doi.org/10.1175/JCLI-D-16-0644.1, 2017.

Atmospheric
Measurement
Techniques
Discussions

Open Access
EGU

Shupe, M. D. and Intrieri, J. M.: Cloud Radiative Forcing of the Arctic Surface: The Influence of Cloud Properties, Surface Albedo, and Solar Zenith Angle, 17, 13, https://doi.org/10.1175/1520-0442(2004)017<0616:CRFOTA>2.0.CO;2, 2004.

Shupe, M. D., Turner, D. D., Walden, V. P., Bennartz, R., Cadeddu, M. P., Castellani, B. B., Cox, C. J., Hudak, D. R., Kulie, M. S., Miller, N. B., Neely, R. R., Neff, W. D., and Rowe, P. M.: High and Dry: New Observations of Tropospheric and Cloud Properties above the Greenland Ice Sheet, 94, 169–186, https://doi.org/10.1175/BAMS-D-11-00249.1, 2013.

Stephens, G. L., Vane, D. G., Tanelli, S., Im, E., Durden, S., Rokey, M., Reinke, D., Partain, P., Mace, G. G., Austin, R., L'Ecuyer, T., Haynes, J., Lebsock, M., Suzuki, K., Waliser, D., Wu, D., Kay, J., Gettelman, A., Wang, Z., and Marchand, R.: CloudSat mission: Performance and early science after the first year of operation, 113, https://doi.org/10.1029/2008JD009982, 2008.

Stroeve, J. C., Serreze, M. C., Holland, M. M., Kay, J. E., Maslanik, J., and Barrett, A. P.: The Arctic's rapidly shrinking sea ice cover: a research synthesis, Climatic Change, 110, 1005–1027, https://doi.org/10.1007/s10584-011-0101-1, 2012.

Stubenrauch, C. J., Rossow, W. B., Kinne, S., Ackerman, S., Cesana, G., Chepfer, H., Girolamo, L. D., Getzewich, B., Guignard, A., Heidinger, A., Maddux, B. C., Menzel, W. P., Minnis, P., Pearl, C., Platnick, S., Poulsen, C., Riedi, J., Sun-Mack, S., Walther, A., Winker, D., Zeng, S., and Zhao, G.: ASSESSMENT OF GLOBAL CLOUD DATASETS FROM SATELLITES, 20, 2013.

Stubenrauch W. B. Rossow, and S. Kinne, 2012: Assessment of global cloud datasets from satellites: A project of the World Climate Research Programme Global Energy and Water Cycle Experiment (GEWEX) Radiation Panel. WCRP Rep. 23/2012, 176 pp. [Available online at www.wcrp-climate.org/documents/GEWEX Cloud_Assessment_2012.pdf.]

Taylor, K. E., Crucifix, M., Braconnot, P., Hewitt, C. D., Doutriaux, C., Broccoli, A. J., Mitchell, J. F. B., and Webb, M. J.: Estimating Shortwave Radiative Forcing and Response in Climate Models, 20, 2530–2543, https://doi.org/10.1175/JCLI4143.1, 2007.

Vaillant de Guélis, T., Chepfer, H., Noel, V., Guzman, R., Dubuisson, P., Winker, D. M., and Kato, S.: The link between outgoing longwave radiation and the altitude at which a spaceborne lidar beam is fully attenuated, Atmos. Meas. Tech., 10, 4659–4685, https://doi.org/10.5194/amt-10-4659-2017, 2017a.

Vaillant de Guélis, T., Chepfer, H., Noel, V., Guzman, R., Winker, D. M., and Plougonven, R.: Using Space Lidar Observations to Decompose Longwave Cloud Radiative Effect Variations Over the Last Decade: Space lidar decomposes LWCRE variations, Geophys. Res. Lett., 44, 11,994-12,003, https://doi.org/10.1002/2017GL074628, 2017b.

Vaillant de Guélis, T., Chepfer, H., Guzman, R., Bonazzola, M., Winker, D. M., and Noel, V.: Space lidar observations constrain longwave cloud feedback, Sci Rep, 8, 16570, https://doi.org/10.1038/s41598-018-34943-1, 2018.

Van Tricht, K., Lhermitte, S., Lenaerts, J. T. M., Gorodetskaya, I. V., L'Ecuyer, T. S., Noël, B., van den Broeke, M. R., Turner, D. D., and van Lipzig, N. P. M.: Clouds enhance Greenland ice sheet meltwater runoff, Nat Commun, 7, 10266, https://doi.org/10.1038/ncomms10266, 2016.

Winker, D. M., Pelon, J., Jr, J. A. C., Ackerman, S. A., Charlson, R. J., Colarco, P. R., Flamant, P., Fu, Q., Hoff, R. M., Kittaka, C., Kubar, T. L., Treut, H. L., Mccormick, M. P., Mégie, G., Poole, L., Powell, K., Trepte, C., Vaughan, M. A., and Wielicki, B. A.: A Global 3D View of Aerosols and Clouds, 20, 2010.

Zelinka, M. D., Klein, S. A., and Hartmann, D. L.: Computing and Partitioning Cloud Feedbacks Using Cloud Property Histograms. Part I: Cloud Radiative Kernels, J. Climate, 25, 3715–3735, https://doi.org/10.1175/JCLI-D-11-00248.1, 2012a.

Zelinka, M. D., Klein, S. A., and Hartmann, D. L.: Computing and Partitioning Cloud Feedbacks Using Cloud Property
825   Histograms. Part II: Attribution to Changes in Cloud Amount, Altitude, and Optical Depth, J. Climate, 25, 3736–3754,
https://doi.org/10.1175/JCLI-D-11-00249.1, 2012b.
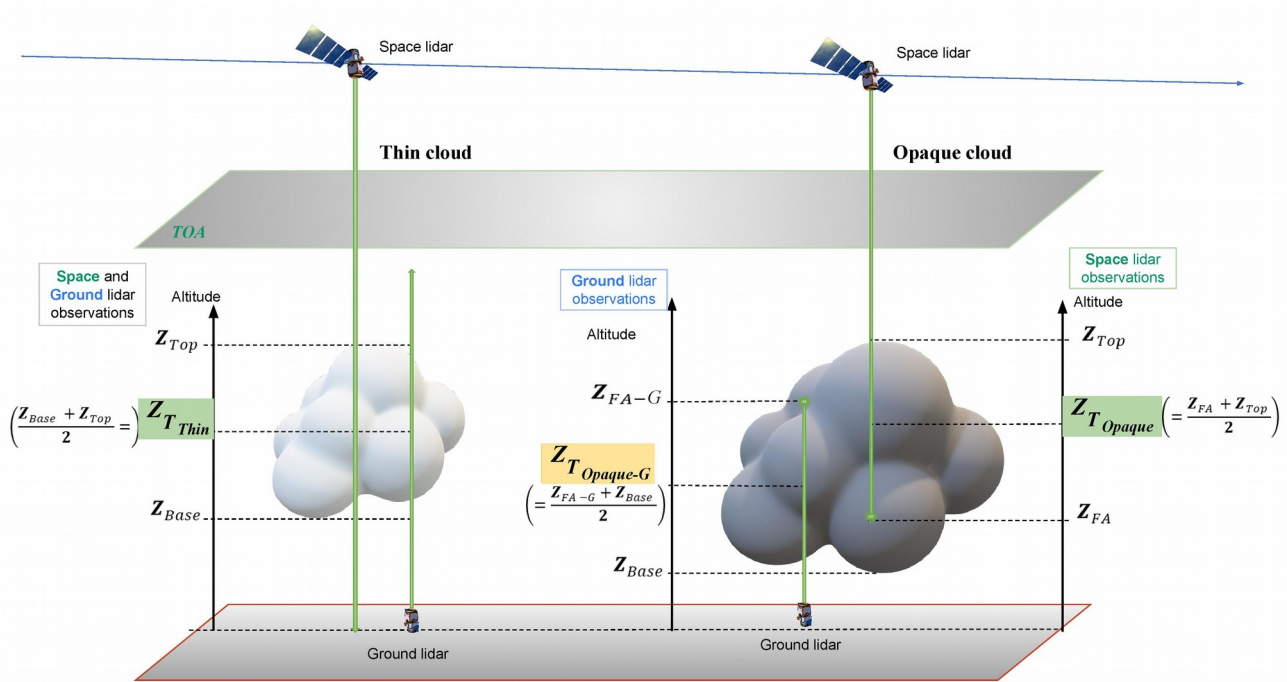
830

Figure 1: Schematic of cloud altitudes seen from space lidar and from a ground based lidar in an atmospheric column containing thin cloud only (left) and opaque cloud only (right). The altitudes used to retrieve the surface LW CRE from CALIPSO–GOCCP are reported in green.
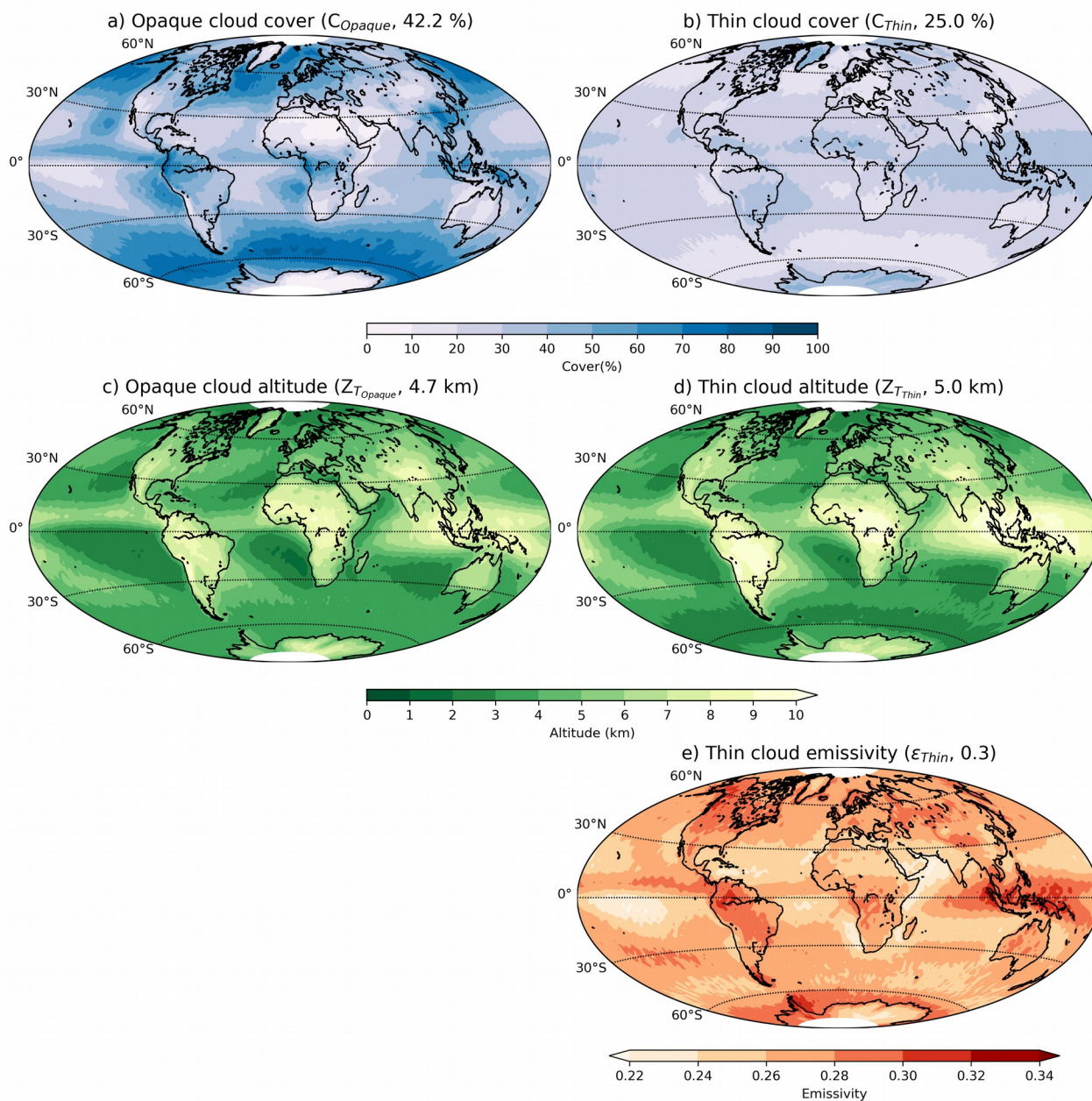
Figure 2: Maps of a) opaque cloud cover C_{Opaque}**, b) thin cloud cover** C_{Thin}**, c) opaque cloud altitude** $Z_{T_{Opaque}}$**, d) thin cloud altitude** $Z_{T_{Thin}}$ **and e) thin cloud emissivity** ε_{Thin}**. Global mean are reported in parentheses. Build from CALIPSO–GOCCP v3.1.2 over 2008–2020.**
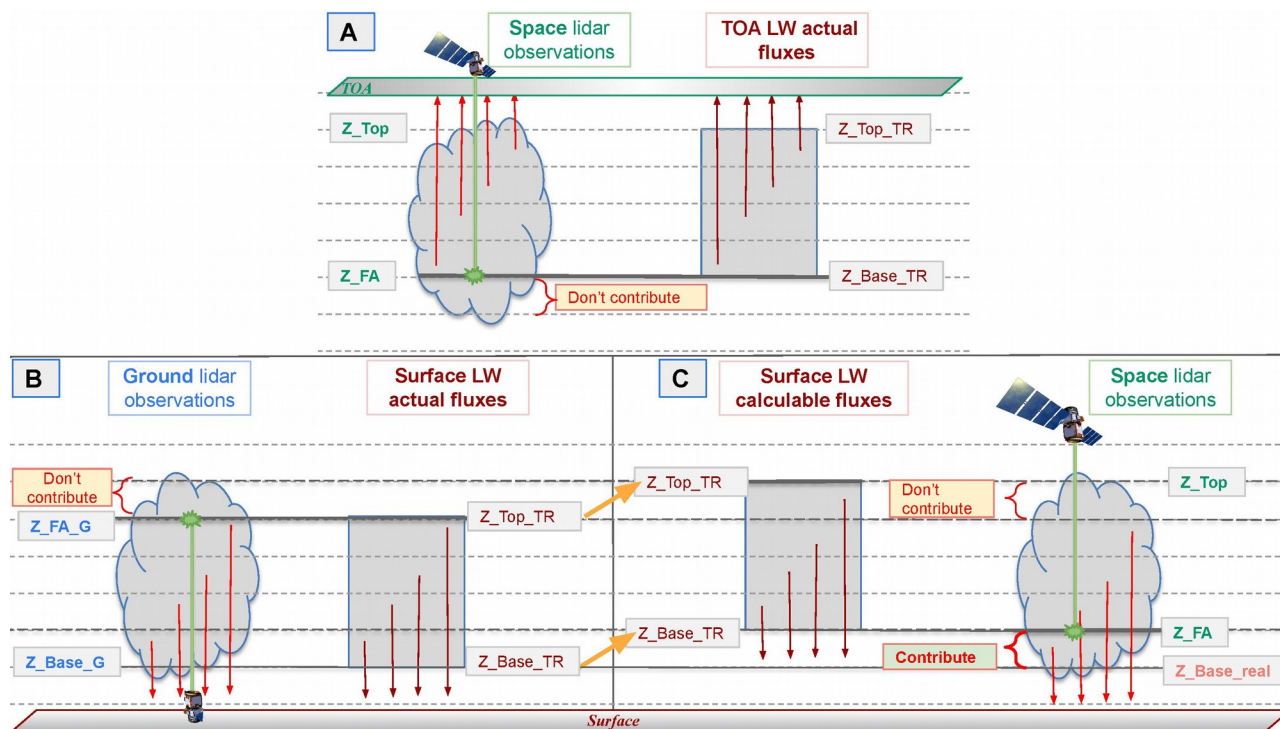
Figure 3: Schematic of cloud altitudes seen from lidars and the radiative transfer computation associated : A) altitudes seen from space lidar observations (left) and radiative transfer computation for TOA LW fluxes (right), B) altitudes seen from ground lidar observations (left) and radiative transfer computation for surface LW fluxes (right), and C) altitudes seen from space lidar observations (right) and radiative transfer computation for surface LW fluxes (left).

Atmospheric
Measurement
Techniques
Open Access
Discussions
EGU
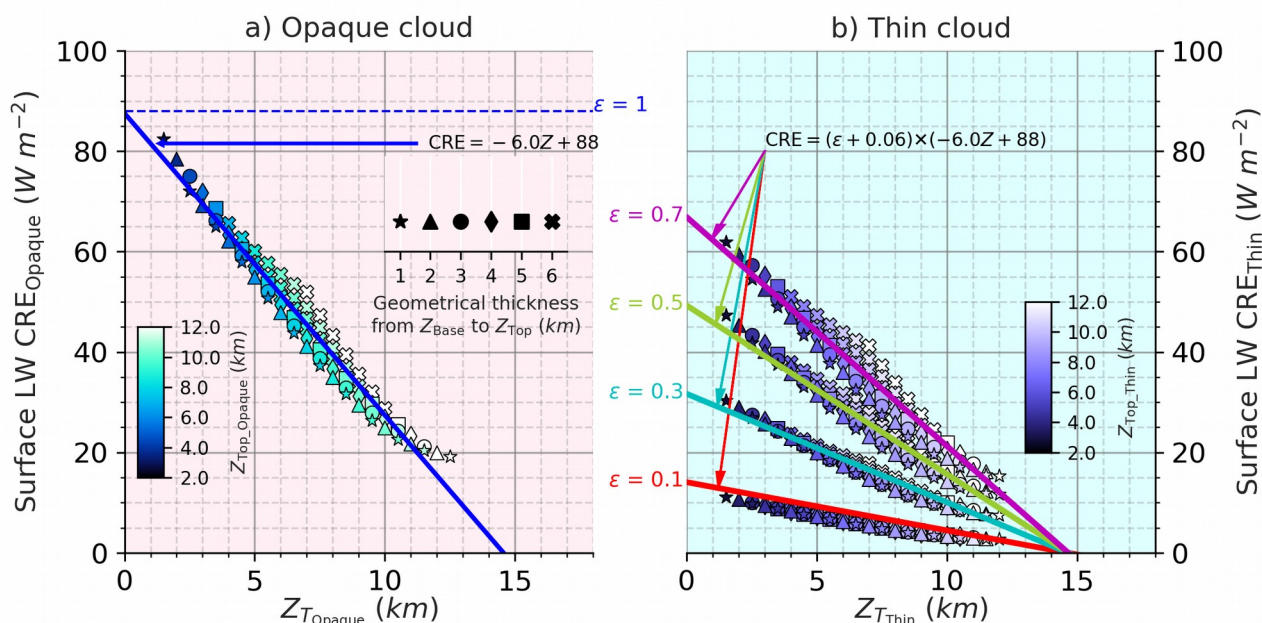
Figure 4: Linear relationships derived from 1D radiative transfer computations between the surface LW CRE and the cloud altitude for a single overcast column containing: a) an opaque cloud above a thin cloud, both moving in altitude, and b) a thin cloud of emissivity 0.1 (red), 0.3 (cyan), 0.5 (green) and 0.7 (pink). These linear relationships (solid lines) are derived from direct radiative transfer computations (dots). Each dot represents the result of one radiative transfer computation. The color of dots represents the cloud top altitude (2 km [dark] – 13 km [bright]) and the size of dots the geometrical thickness from the cloud base to cloud top (1 km [small] – 6 km and above [large]). The atmospheric state is taken from ERA Interim reanalysis for January at a latitude of 39° N over ocean.
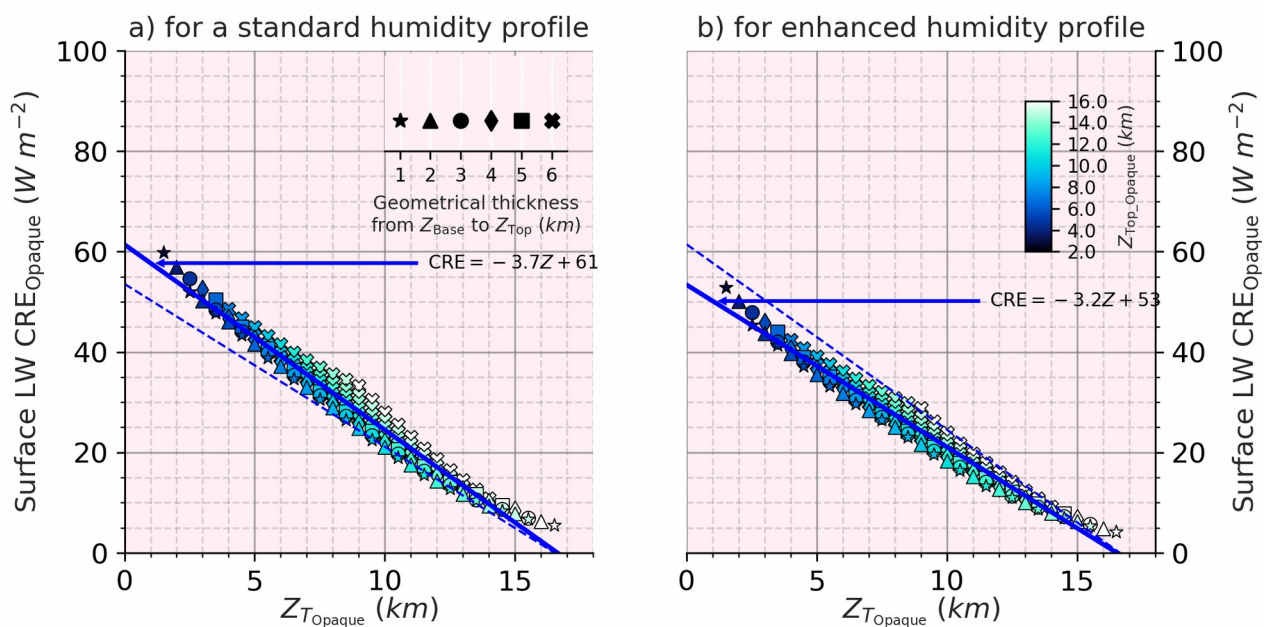
Figure 5: Same as Fig. 4a for: a) a standard humidity profile and b) enhanced humidity profile. Both in the tropics [30° S–30° N].

Atmospheric
Measurement
Techniques
Discussions

Open Access

EGU
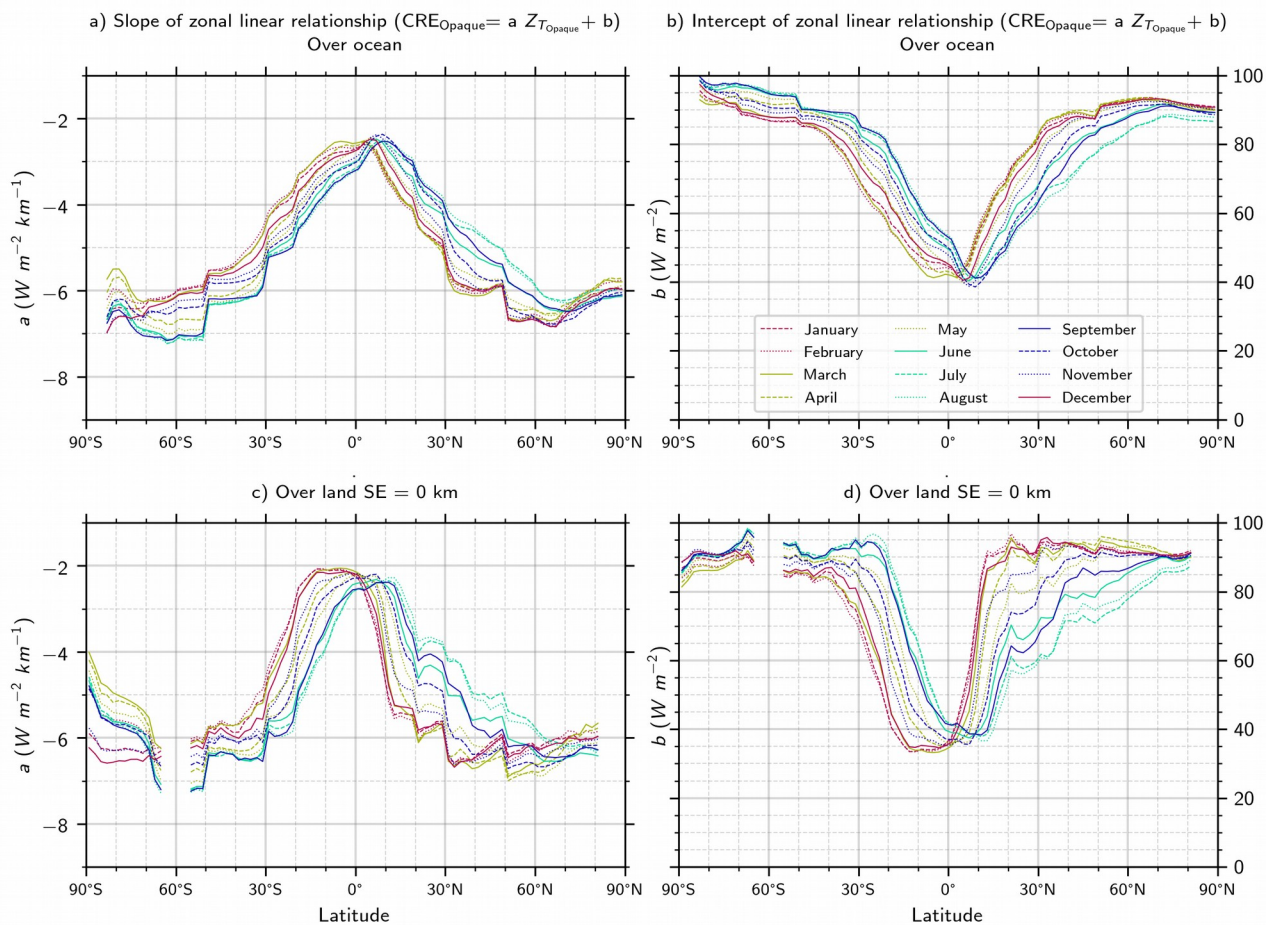
860

Figure 6: Coefficients of the linear relationships derived from 1D radiative transfer computations between the surface LW CRE and the cloud altitude for all latitudes and seasons : a) the slope of the relationships over ocean, b) intercept of the relationships over ocean, c) the slope of the relationships over land and, d) intercept of the relationships over land.
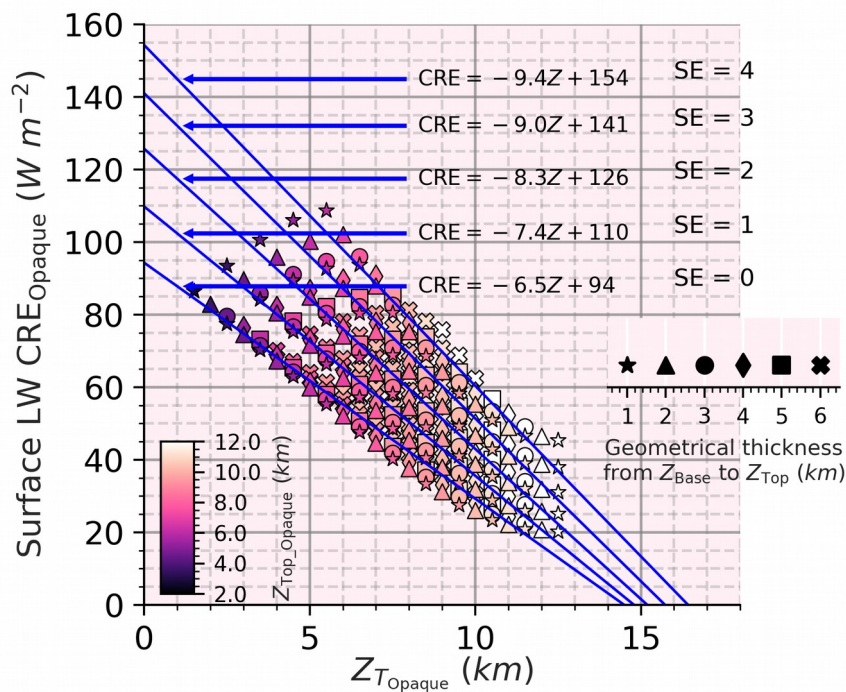
Figure 7: Sensitivity of the surface LW opaque CRE to the surface elevation (SE) : Same as Fig. 4a but over land and for different values of SE : SE = 0 (sea level), SE = 1 km, SE = 2 km, SE = 3 km, SE = 4 km for January at a latitude of 39° N.
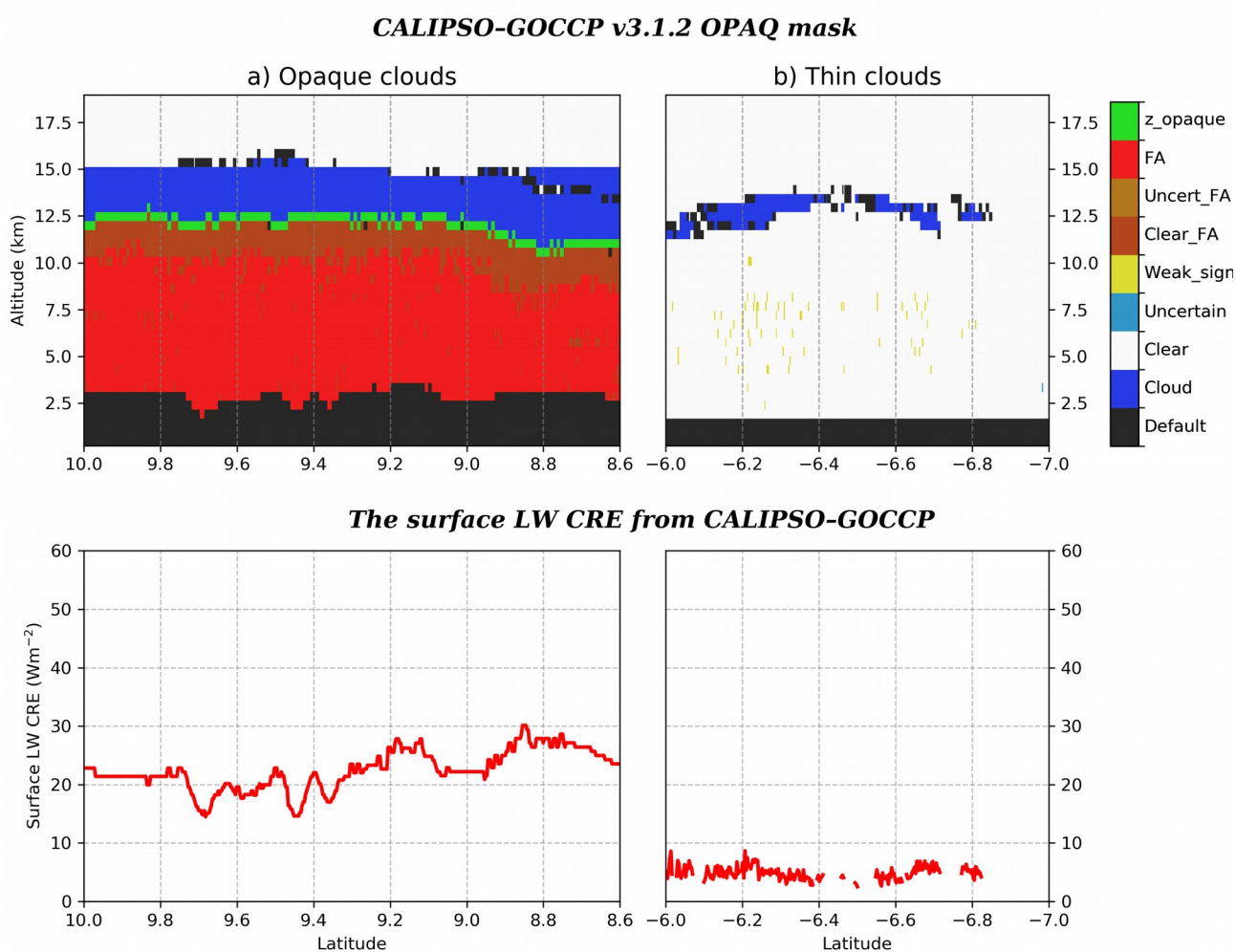
Figure 8: Pieces of CALIPSO orbit passing over Africa the 11th August 2010 at 23 h 02 min 38 sec. Opaque clouds (left column) and, thin clouds (right column). Top line) Vertical feature mask from the product CALIPSO–GOCCP–OPAQ (Guzman et al., 20017), the black areas below 4km correspond to land. Bottom line) Surface LW CRE from CALIPSO–GOCCP.

895
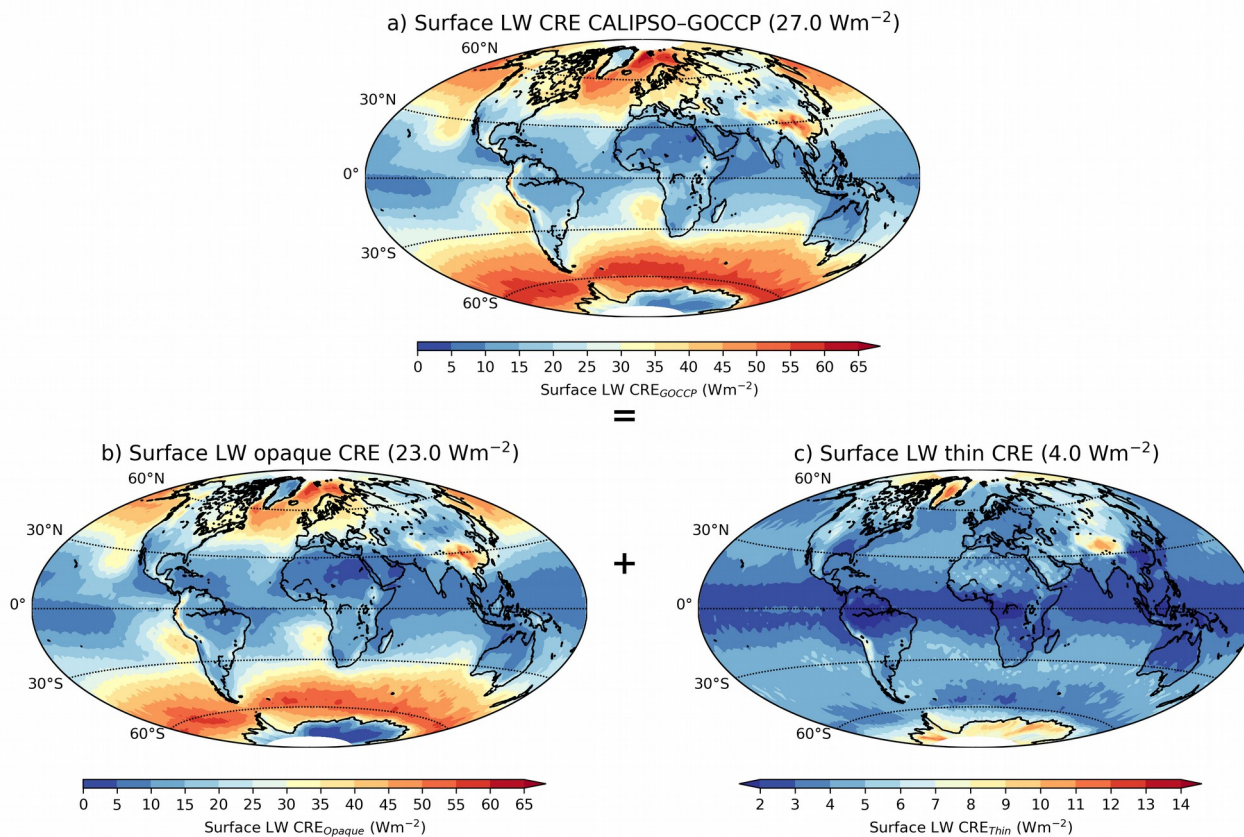
Figure 9: Maps of the surface LW CRE: a) all clouds, b) opaque clouds, and c) thin clouds. These surface LW CRE are built from CALIPSO–GOCCP v3.1.2 dataset (Fig. 2) and radiative transfer computations (Figs. 4–7, A1). The surface LW CRE is averaged over 2008–2020. Note that the color scale is different in c).

900
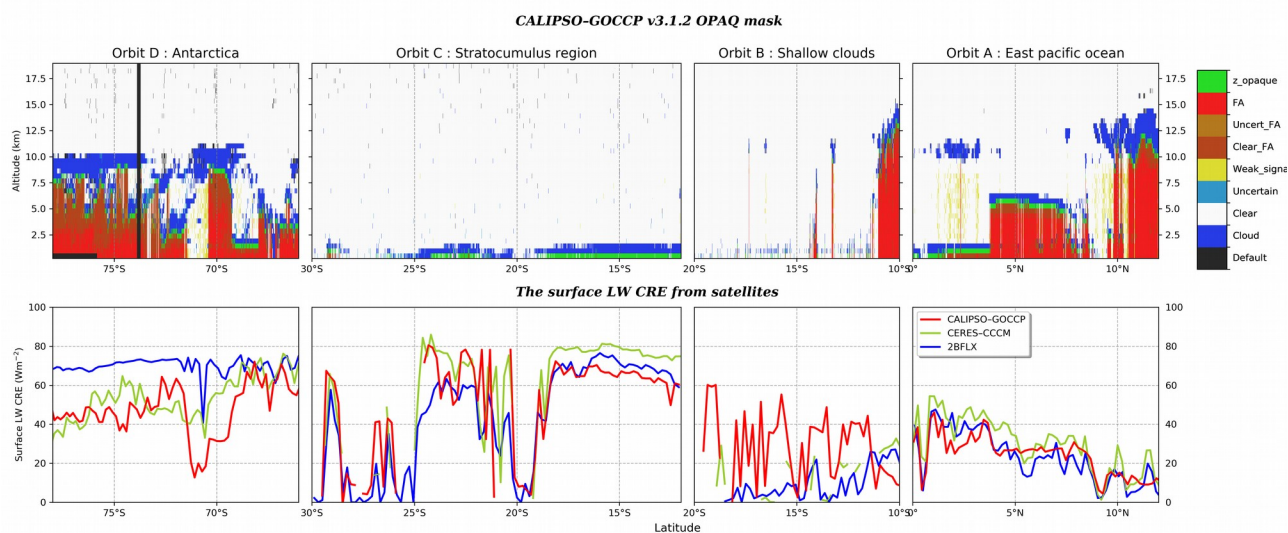
905 **Figure 10: Pieces of CALIPSO orbits passing over: A) east Pacific ocean the 17th October at 8 h 21 min 48 sec, B) shallow clouds region in the Pacific ocean the 5th April at 12 h 55 min 34 sec, C) stratocumulus region the 13th July at 6 h 48 min 37 sec and D) Antarctica the 21st September at 3 h 9 min 46 sec all for the year 2008. Top line) Vertical feature mask from the product CALIPSO–GOCCP–OPAQ (Guzman et al., 20017), the black areas below 4km correspond to land. Bottom line) Surface LW CRE of the three satellite products. The location of the pieces of orbit (A, B, C, D) are reported in Figure 12.c.**
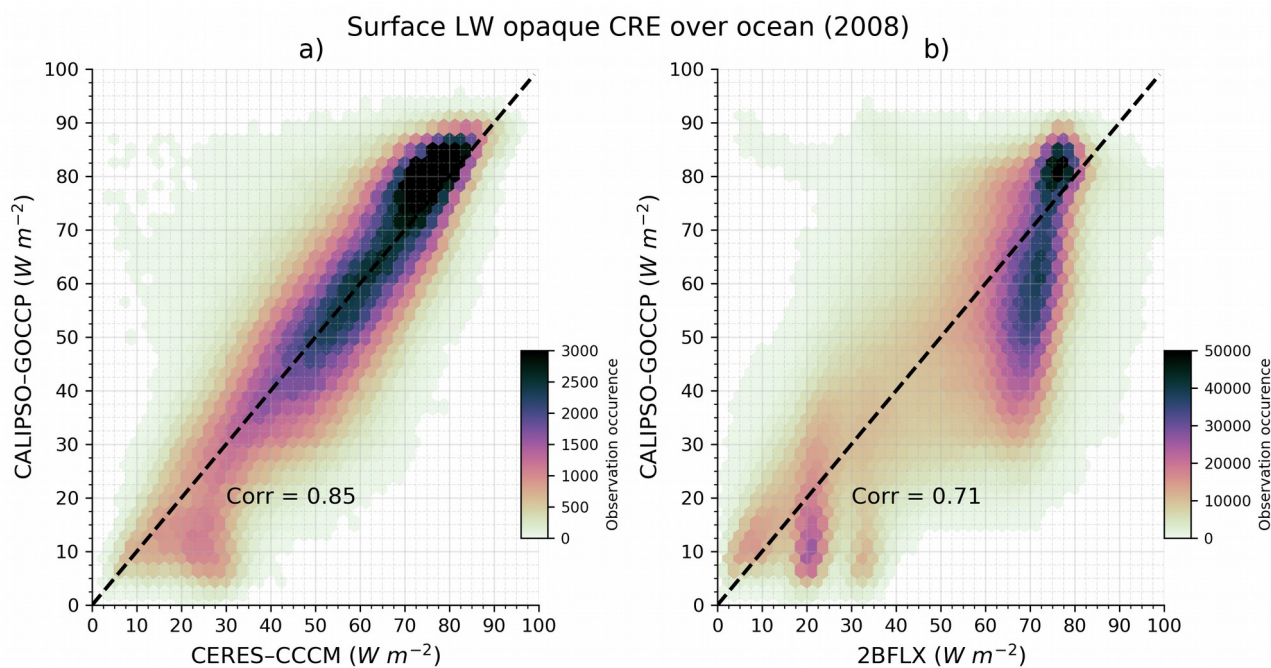
Figure 11: Instantaneous collocated surface LW opaque CRE at footprint scale: a) CALIPSO–GOCCP as a function of CERES–CCCM , b) CALIPSO–GOCCP as a function of 2BFLX. We only consider CERES (CloudSat) footprints where all CALIPSO footprints falling within the CERES (CloudSat) footprints are opaque and which contain at least 40 (10) profiles. Based on collocated observations over ocean in 2008.

915
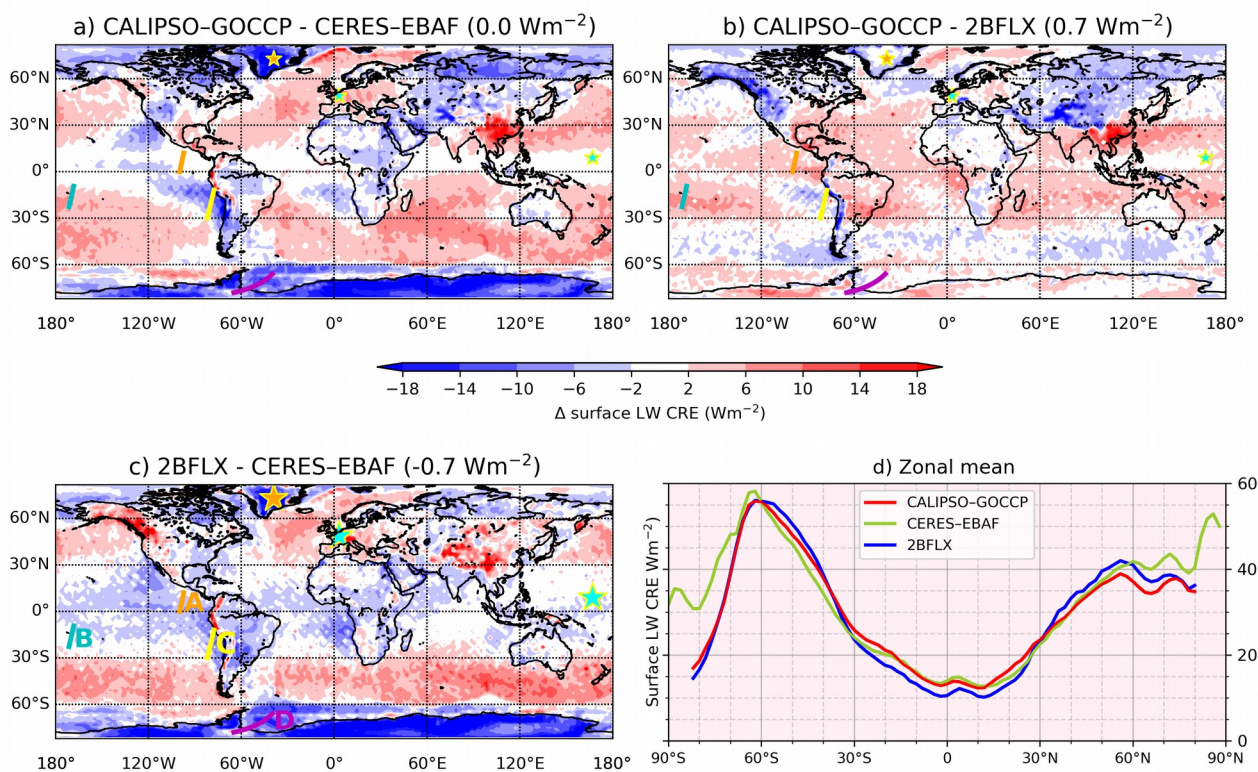
Figure 12: Maps of differences in the surface LW CRE a) CALIPSO–GOCCP minus CERES–EBAF, b) CALIPSO–GOCCP minus 2BFLX, c) 2BFLX minus CERES–EBAF, and d) zonal means of the three satellite products. Data are averaged over 2008–2010. Locations of the three ground-based sites and pieces of orbits are reported in map c).

Atmospheric
Measurement
Techniques
Open Access
Discussions
EGU
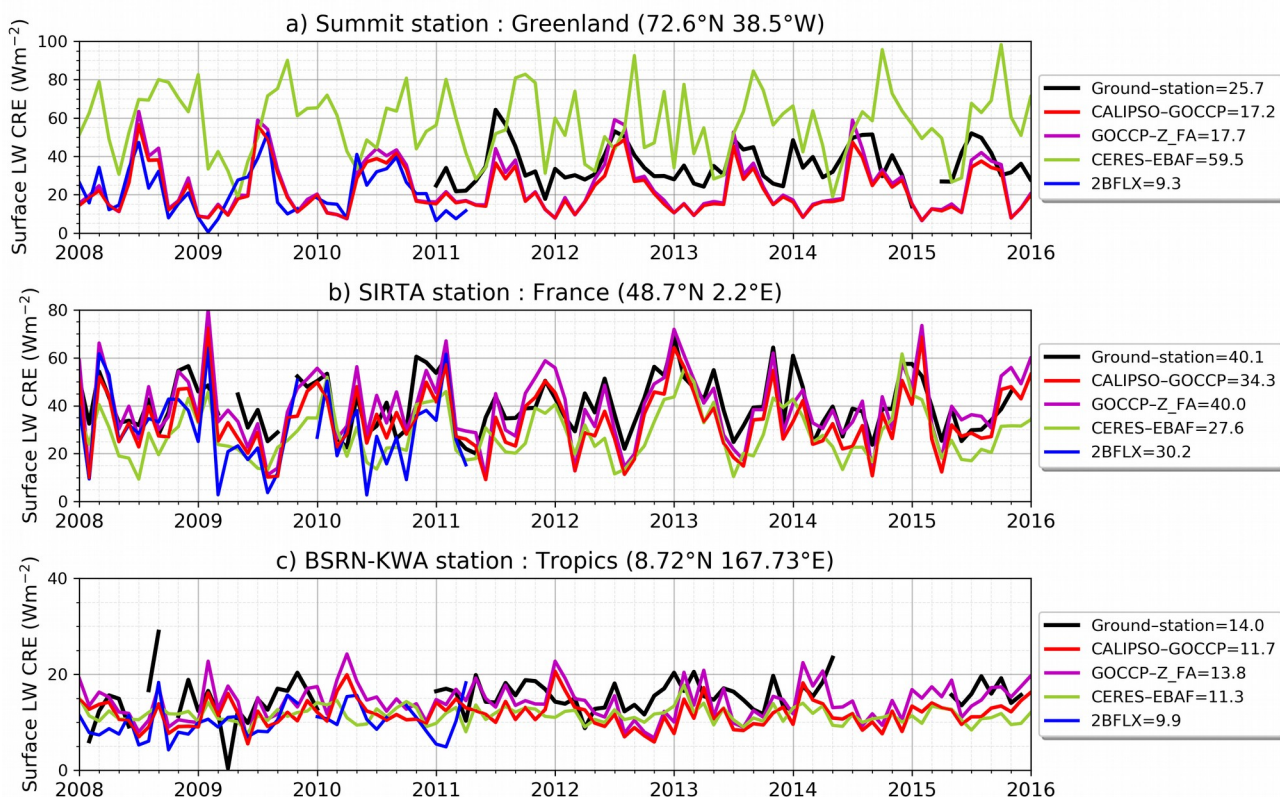
Figure 13: Comparisons between the surface LW CRE derived from ground-stations measurements and from satellites in three locations : a) polar region at Greenland Summit site, b) mid-latitudes at SIRTA site, and c) tropics at KWA site. Mean values reported in the legend are computed only over the time period when all products are available e.g. only three months (JFM 2011) for Greenland Summit mean values. The locations of the three sites are reported in Fig. 12c. Note that the y-axis scale is different in each subplot.

930
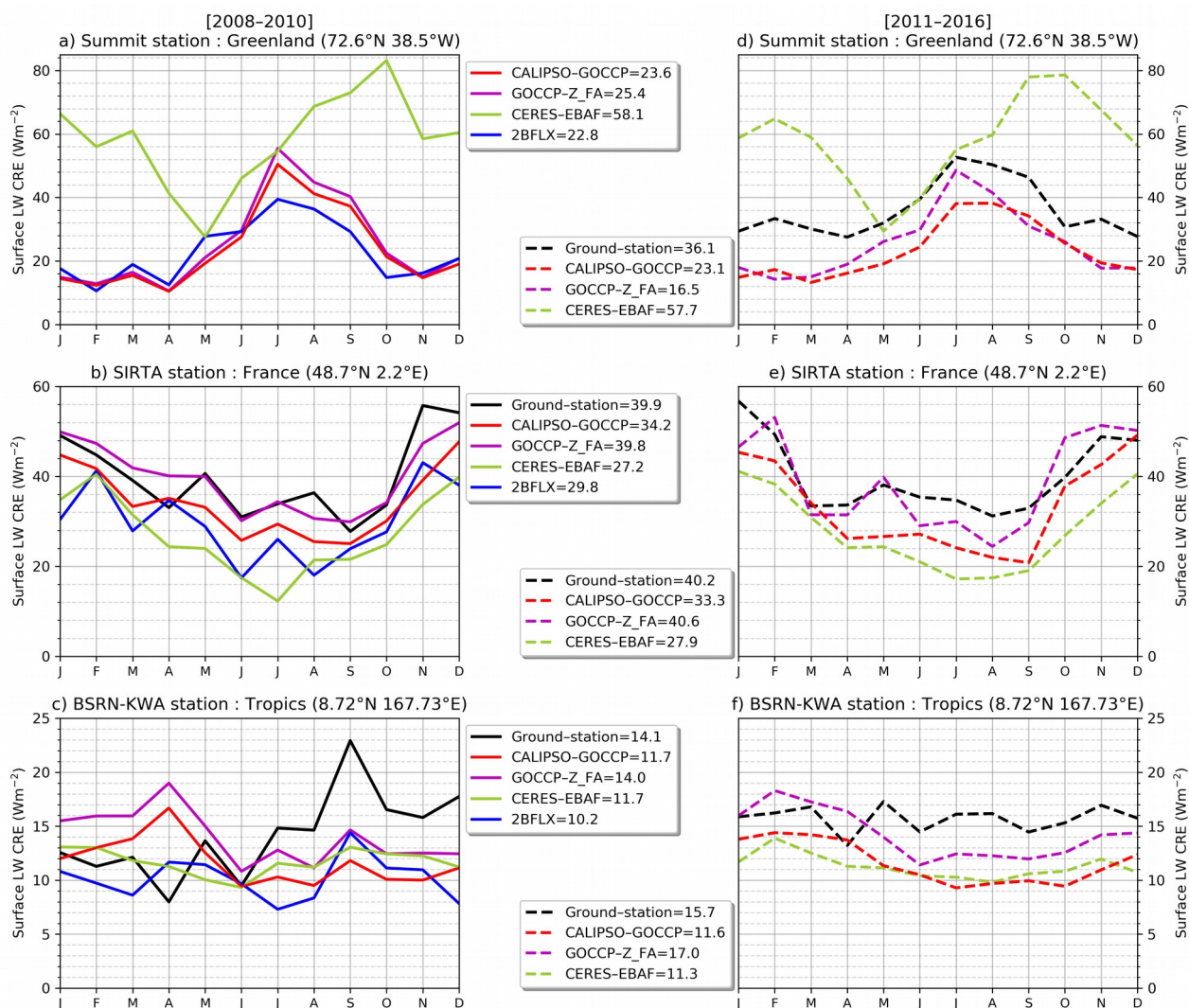
Figure 14: Same as Fig. 13 but in mean seasonal cycles. Left column corresponds to 2008–2010 and right column corresponds to 2011–2016. Note that the y-axis scale is different in each subplot.
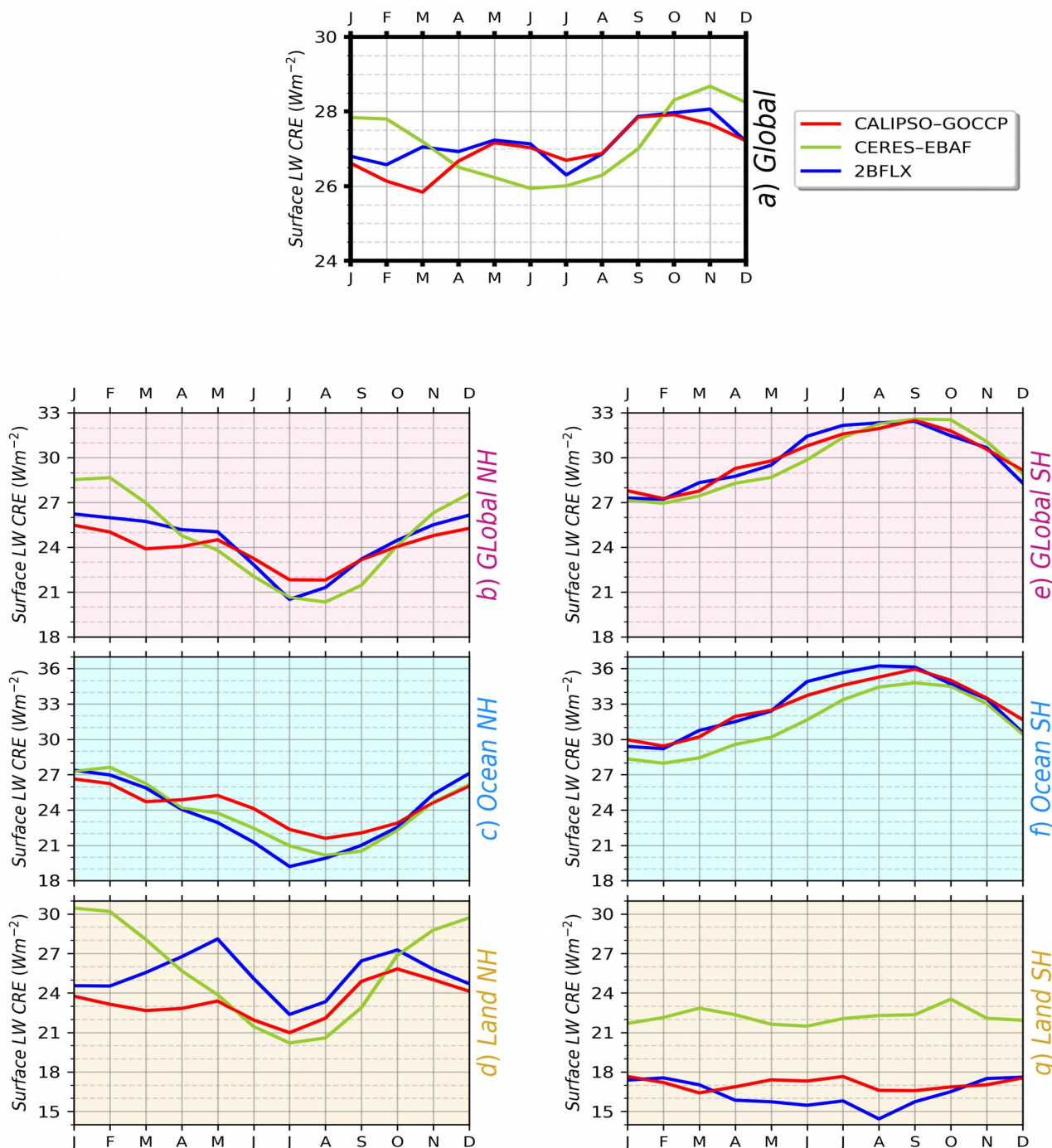
Figure 15: Seasonal cycle of the surface LW CRE derived from satellites in: a) global , b) all NH, c) ocean NH, d) land NH, e) all SH, f) ocean SH, g) land SH. CALIPSO–GOCCP and CERES–EBAF are averaged over 2008–2020 while 2BFLX is only available over 2008–2010. Note that the y-axis scale is different in each subplot.

940
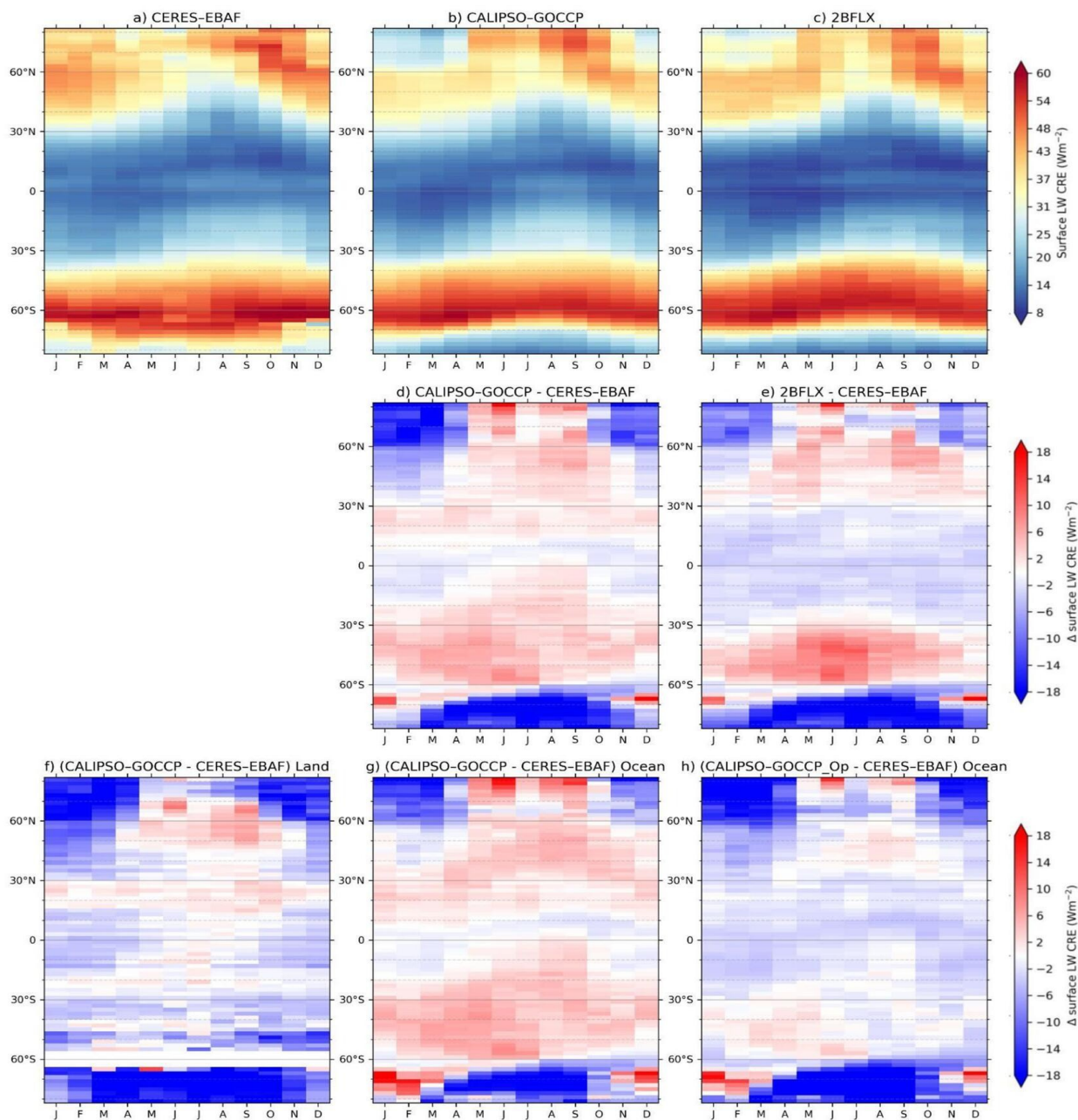
Figure 16: Seasonal evolution of the zonal mean of the surface LW CRE: first line) for each satellite product, second line) differences between satellite products, third line) differences between CALIPSO–GOCCP and CERES–EBAF decomposed into f) land only, g) ocean only, and h) ocean only but using CRE_{Opaque} instead of CRE for CALIPSO–GOCCP.
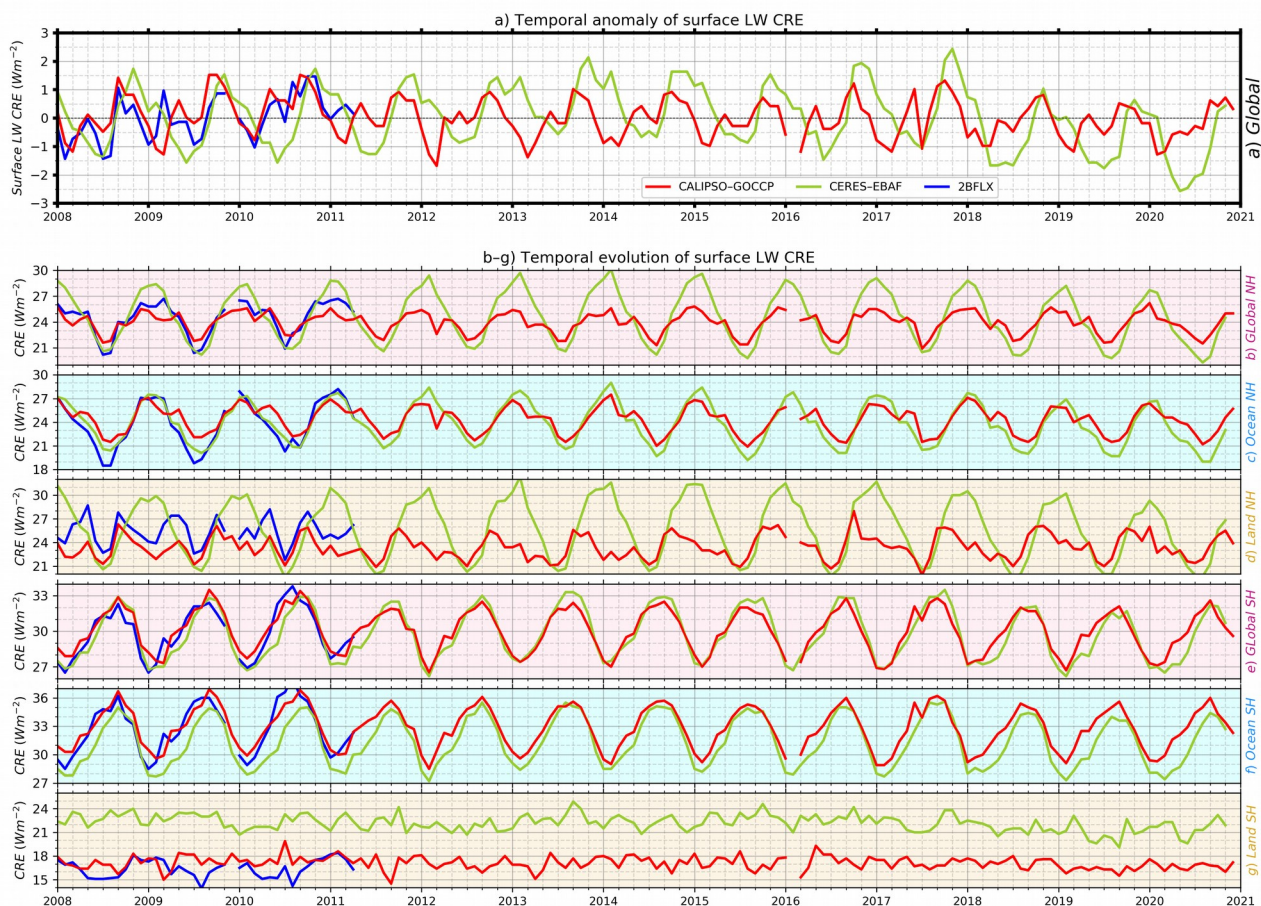
Figure 17: a) Time series of global surface LW CRE anomalies. b-f) Time series of surface LW CREs over all NH, ocean NH, land NH, all SH, ocean SH, land SH. In a) the anomaly is defined as the global average for each month of each product minus its own average over the whole time serie. Note that the y-axis scale is different in each subplot.

Atmospheric
Measurement
Techniques
Open Access
Discussions
EGU
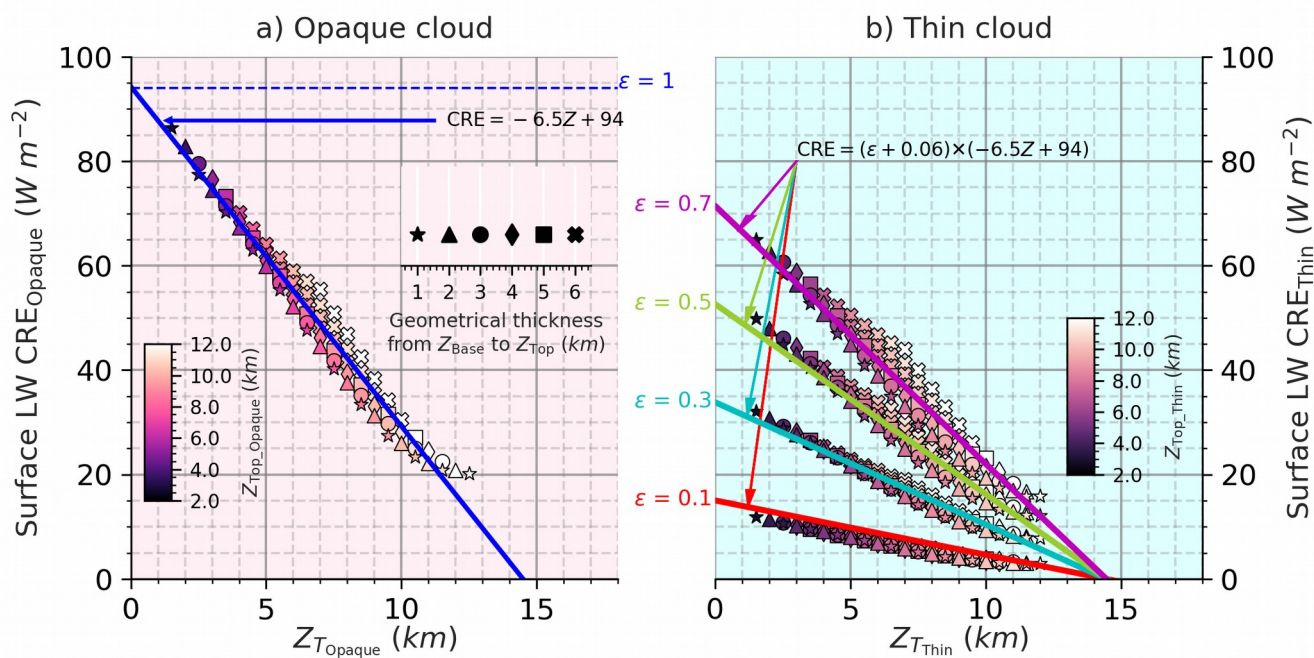
Figure A1: Same as Fig. 4 but over land.

955

Atmospheric
Measurement
Techniques
Discussions

Open Access
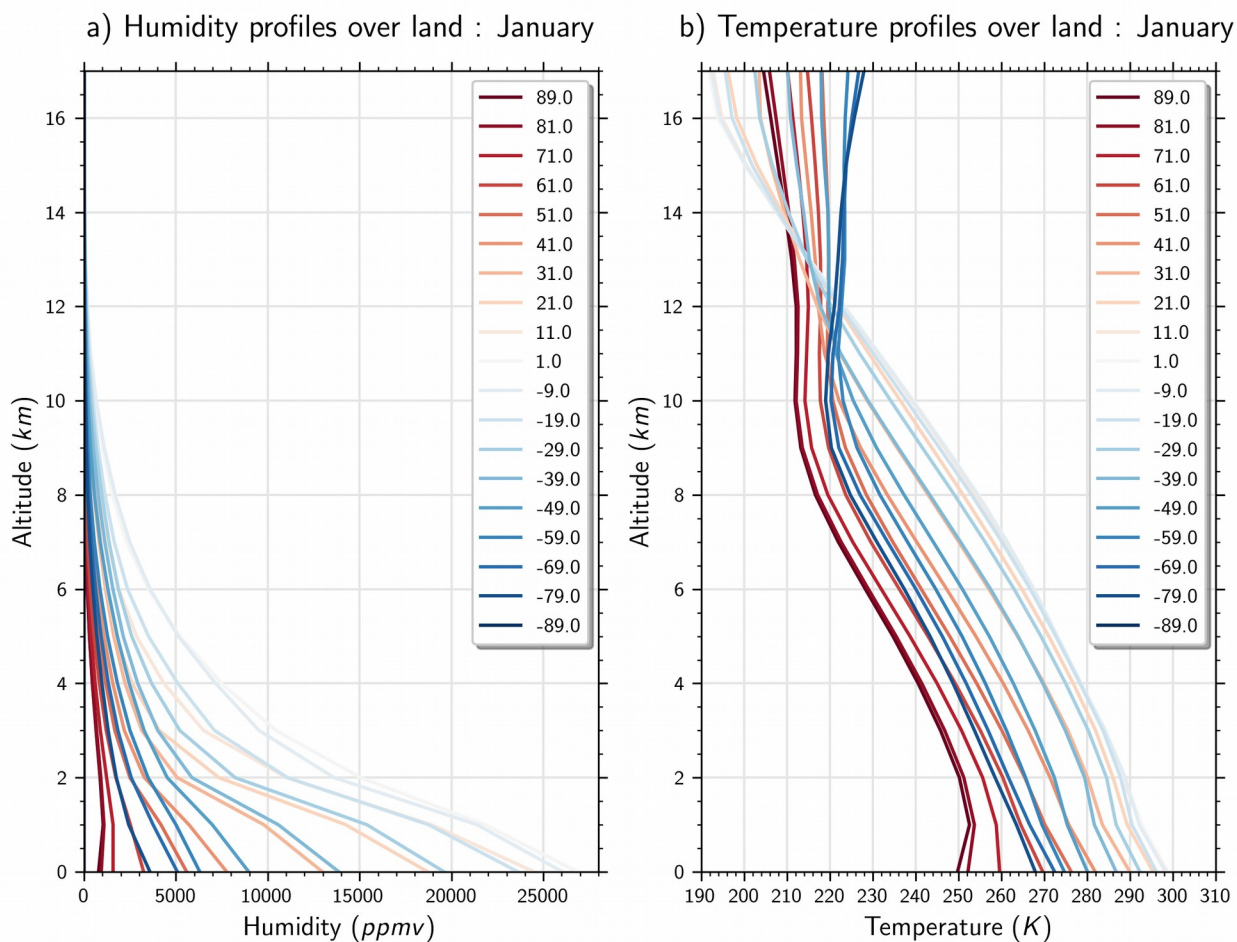
Figure A2: Exemple of ERA Interim atmospheric profiles taken over land in January and averaged over 10° latitude bands.
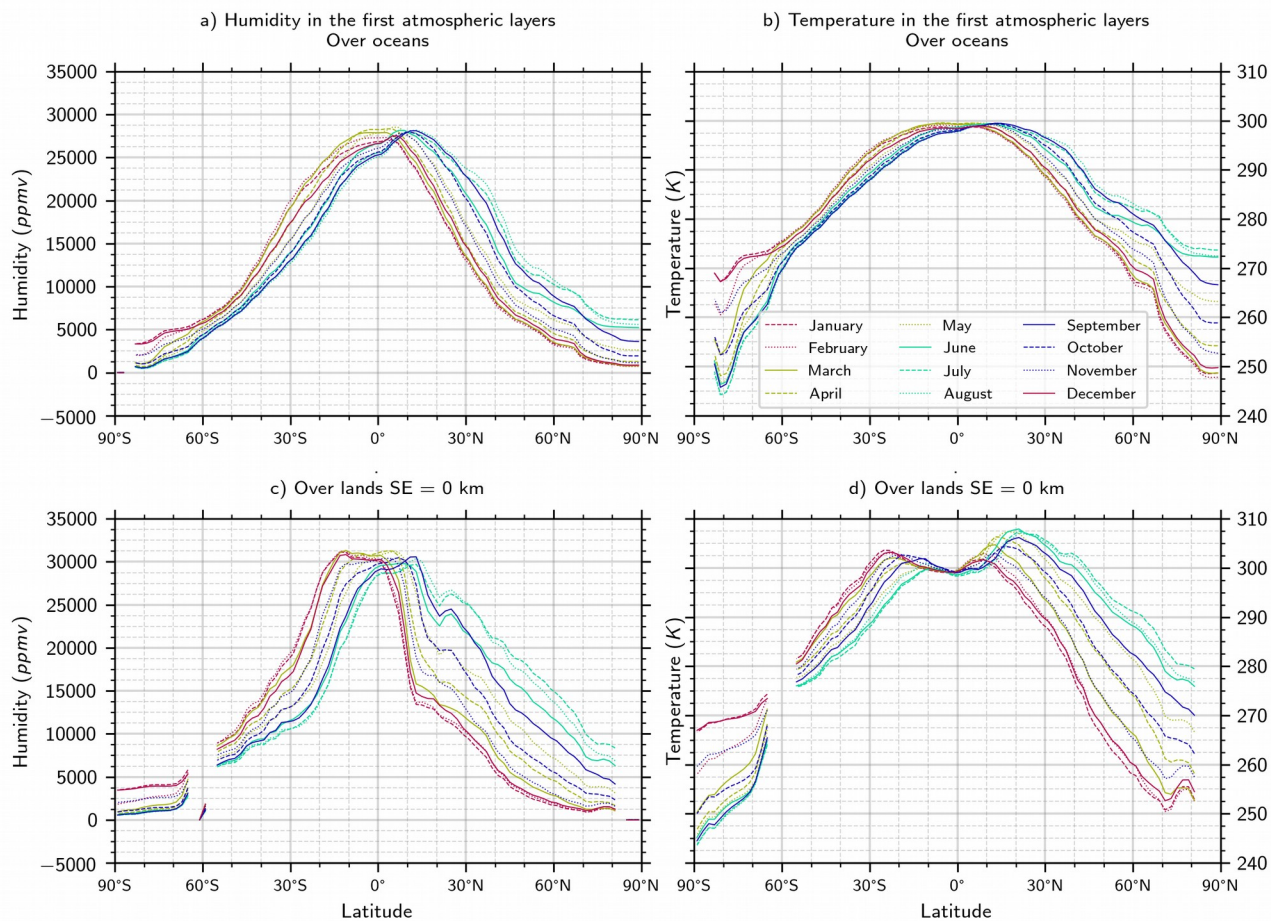
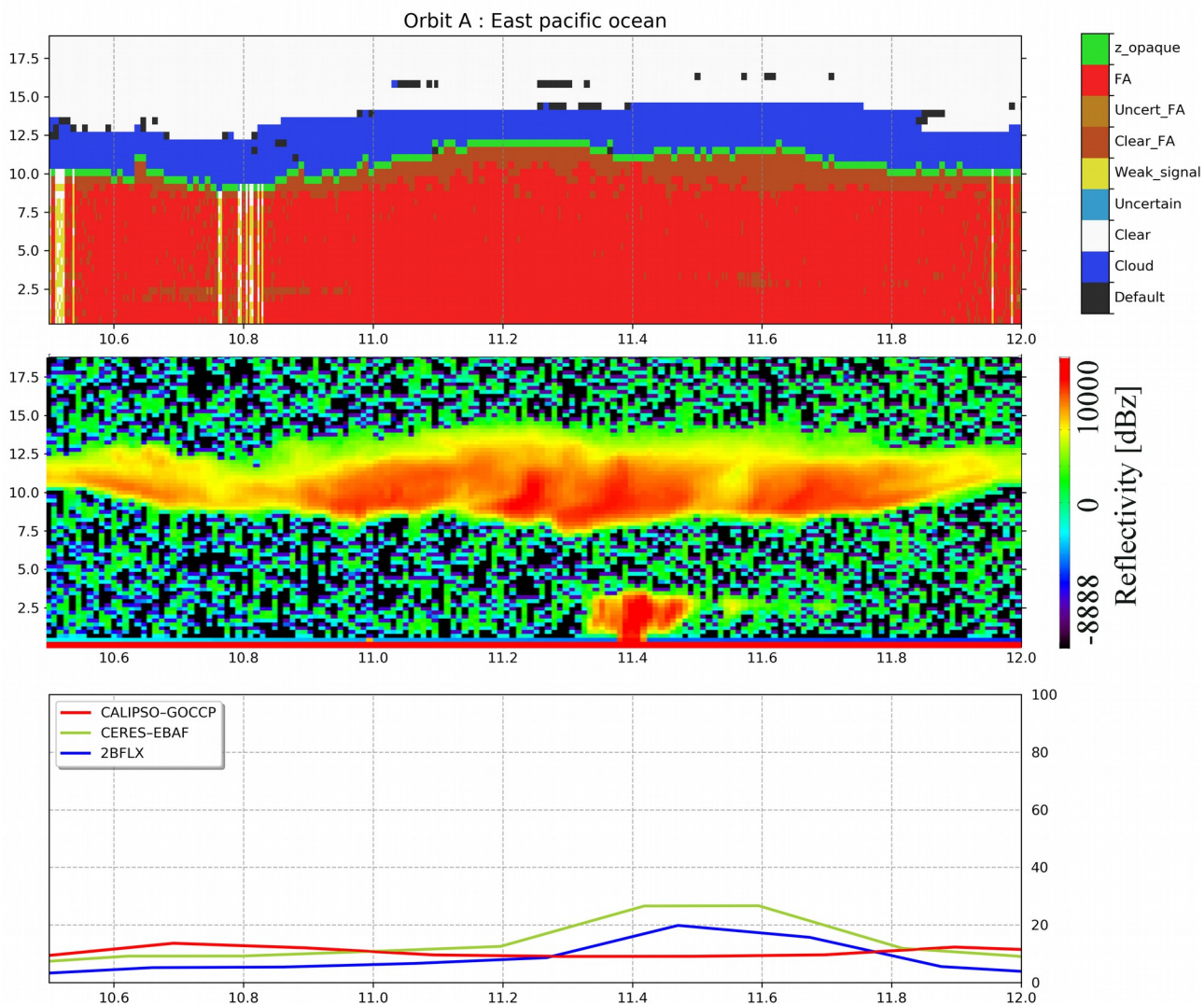**Figure A3: Seasonal and zonal variations of the temperature and humidity in the near surface atmospheric layer (Z < 1 km) from ERA Interim.**
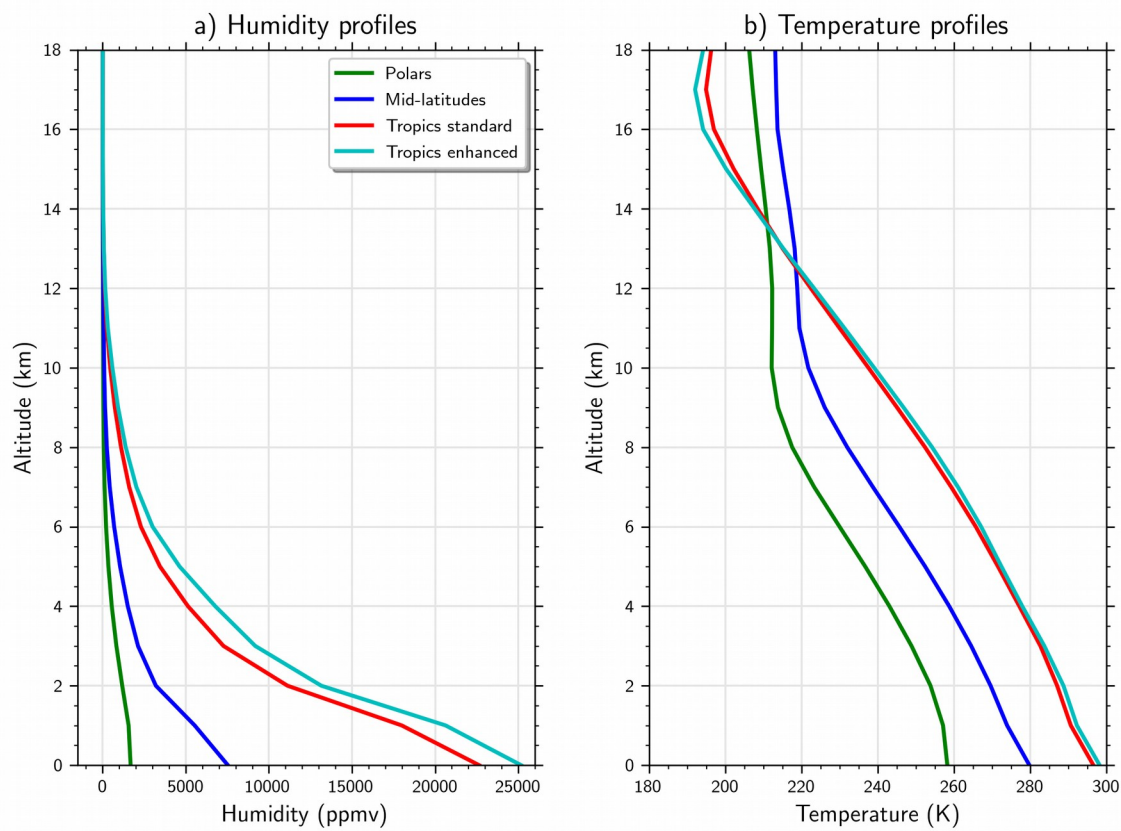
Figure A4: Annual mean profiles of temperature and humidity from ERA Interim.

Figure B1: same as figure 10.A between 10.5° N and 12 °N : a) CALIPSO–GOCCP–OPAQ mask, b) CloudSat reflectivity and c) surface LW CREs.
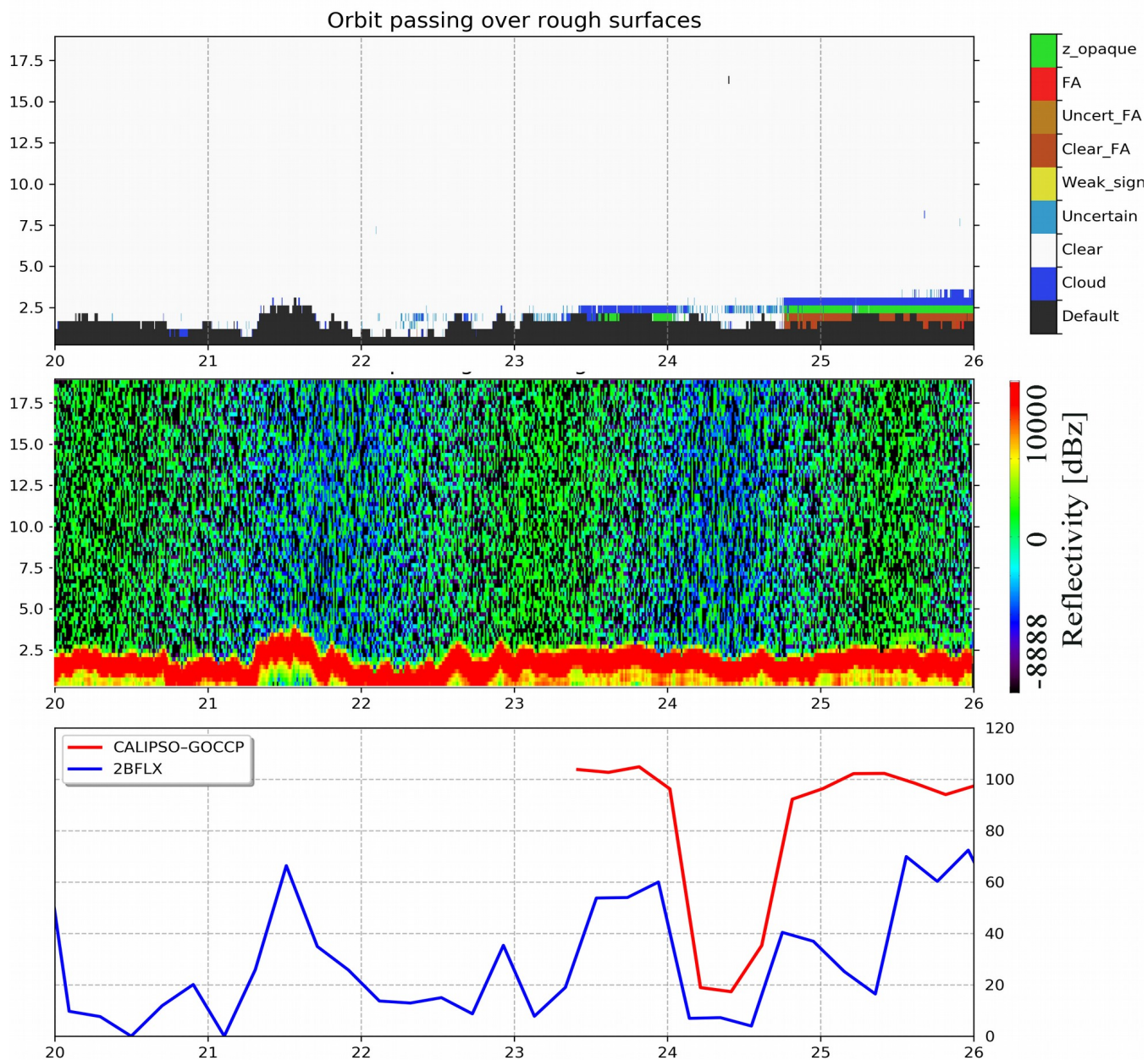
Figure B2: same as fig. B1 but for a piece of orbit passing over China the 10th November 2008 at 18 h 58 min 39 sec,
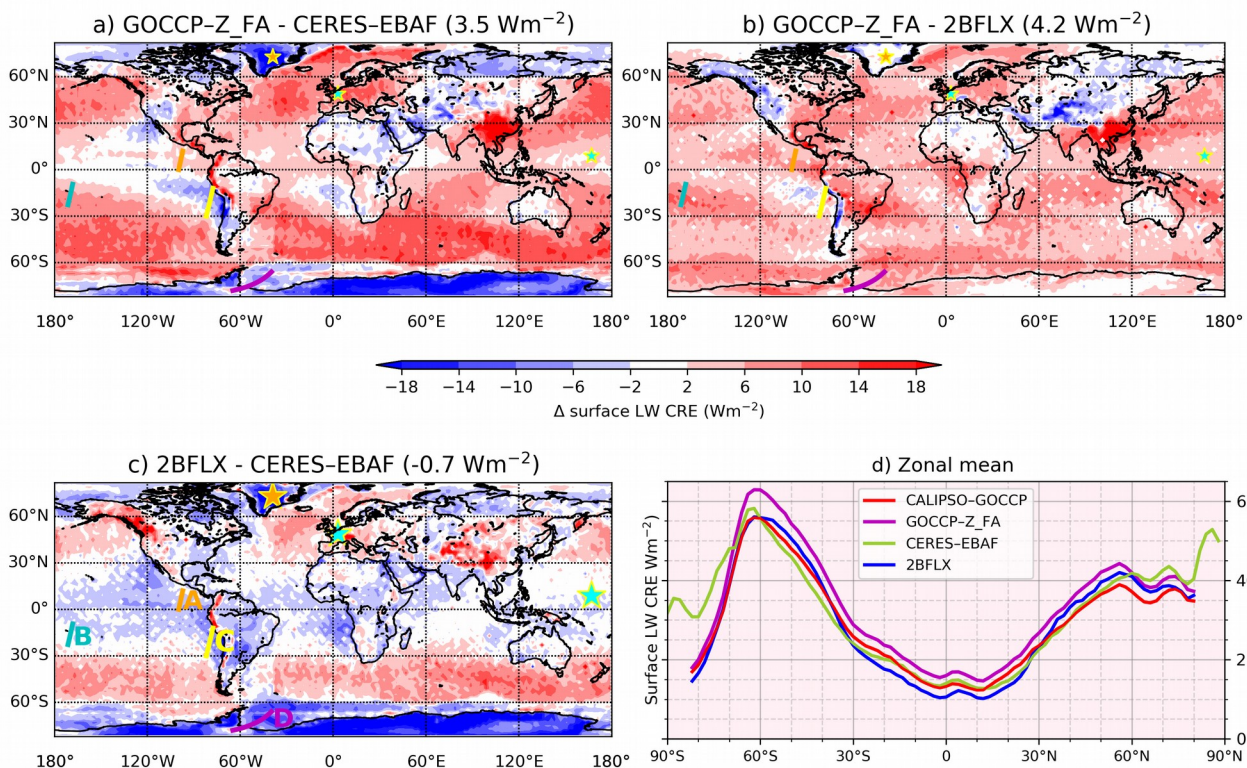
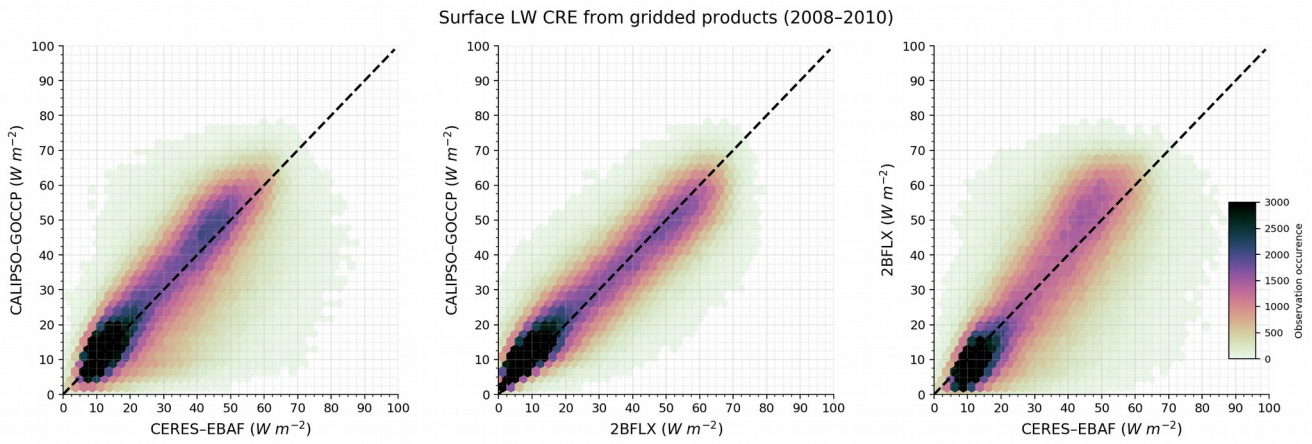Figure B3: same as Fig. 12 but CALIPSO–GOCCP surface LW CRE is retrieved using Z_{FA} instead of $Z_{T_{Opaque}}$.

Atmospheric
Measurement
Techniques
Discussions

Figure B4: Comparison of monthly, 2°×2° gridded surface LW CRE from CALIPSO–GOCCP, CERES–EBAF, and 2BFLX.